

# On Seismic Gradiometric Wave Equation Inversion for Density

Marthe Faber\* and Andrew Curtis

University of Edinburgh, School of Geosciences, Edinburgh, UK

*E-mails:* M.Faber@sms.ed.ac.uk (M.Faber), Andrew.Curtis@ed.ac.uk (A.Curtis)

## Abstract

Material density remains poorly constrained in seismic imaging problems, yet knowledge of density would provide important insight into physical material properties for the interpretation of subsurface structures. We test ambient noise wavefield sensitivities to subsurface density contrasts through spatial and temporal wavefield gradients via Wave Equation Inversion (WEI), a form of seismic gradiometry. Synthetic results for 3D acoustic media suggest that it is possible to estimate relative density structure with WEI by using a full acoustic formulation for wave propagation and gradiometry. We show that imposing a constant density assumption on the medium can be detrimental to subsurface velocity images, whereas the full acoustic formulation assuming variable density improves our knowledge of both material properties. It allows us to estimate density as an additional material parameter, as well as to improve phase velocity estimates by accounting for approximations to the density structure. In 3D elastic media, severe approximations in the governing wave physics are necessary in order to invert for density using only an array of receivers on the free surface. It is then not straightforward to isolate the comparatively weak density signal from the influence of phase velocity using gradiometric WEI. However, by using receivers both at the surface and in the shallow subsurface we show that it is possible to estimate density using fully elastic volumetric WEI.

**Key words:** Inverse theory; Crustal Imaging; Seismic Noise

\*Corresponding author.

## <sup>24</sup> 1 Introduction

<sup>25</sup> Dynamic processes in the Earth's shallow subsurface (top few 100 m) in which rocks, soil, atmospheric gases  
<sup>26</sup> and meteoric water interact are seldom well characterised and understood (Parsekian et al., 2015, Riebe  
<sup>27</sup> et al., 2017). It is of interest for environmental and resource applications to better characterize these chem-  
<sup>28</sup>ical and mechanical processes using information about the heterogeneity in properties of the near-surface,  
<sup>29</sup> so-called critical zone (Anderson et al., 2007). In critical zone studies, bulk density is an important physical  
<sup>30</sup>property as an indicator for soil quality and compaction (Suuster et al., 2011). Lateral density variations  
<sup>31</sup>can reveal information about changes in porosity, fracture distribution and soil weathering (Flinchum et al.,  
<sup>32</sup> 2022). Density is used to inform studies of root growth (Brimhall et al., 1992; Dexter, 2004), water move-  
<sup>33</sup>ment and retention (Huang et al., 2011; Flinchum et al., 2018), as well as carbon and nutrient content in  
<sup>34</sup>soil layers (Nanko et al., 2014). It is therefore of significant interest to be able to estimate near-surface density.

<sup>35</sup>

<sup>36</sup> Direct density measurements can be obtained via auger samples or Geoprobe coring (Holbrook et al., 2014).  
<sup>37</sup> Given that obtaining in-situ measurements of bulk density at any significant depth is time-intensive and  
<sup>38</sup>expensive, it may be preferable to estimate density indirectly. So-called pedotransfer functions are used to  
<sup>39</sup>predict bulk density based on regression models from soil measurement archives for the very shallow subsur-  
<sup>40</sup>face (< 1 m) (Suuster et al., 2011). However, due to the sparsity of borehole samples from deep soil layers,  
<sup>41</sup>few studies are able to estimate bulk density for deeper targets (Qiao et al., 2019). Well logs can be used to  
<sup>42</sup>gain insight on bulk density and to infer porosity of the logged near-surface interval (Fanchi, 2010, Holbrook  
<sup>43</sup>et al., 2019), but remain invasive, localized and again expensive sources of information.

<sup>44</sup>

<sup>45</sup> Geophysical methods complement direct observations. They allow larger and deeper subsurface volumes to  
<sup>46</sup>be investigated, and temporal changes in properties to be monitored (Parsekian et al., 2015). Microgravity  
<sup>47</sup>surveys are directly sensitive to density anomalies and are commonly used for environmental studies of the  
<sup>48</sup>subsurface, e.g., to localize subsurface voids (Tuckwell et al., 2008) or for groundwater monitoring (Piccolroaz  
<sup>49</sup>et al., 2015). However, this data type is strongly impacted by microseismic noise which might overshadow  
<sup>50</sup>small signals related to mass distributions in the near surface (Boddice et al., 2022). Signals from density  
<sup>51</sup>variations in the near surface soil (top 5 m) for example have been shown to be too weak to be detected  
<sup>52</sup>by current gravity instrumentation, leading to lateral variations being obscured by the influence of deeper  
<sup>53</sup>anomalies (Boddice et al., 2019). Furthermore, inversion procedures for subsurface density on the basis of  
<sup>54</sup>gravity data alone are inherently ill-posed (Blom et al., 2017). To reduce the non-uniqueness in solutions,  
<sup>55</sup>gravity measurements must be used in conjunction with other data types such as geological prior knowledge,

56 well-log densities or seismic data to produce realistic density maps (Nabighian et al., 2005).

57

58 Seismic imaging provides another non-invasive alternative to investigate the critical zone. Active methods  
59 such as seismic refraction tomography (Befus et al., 2011; Nielson et al., 2021; Flinchum et al., 2022) and  
60 multi-channel surface wave analysis (Handoyo et al., 2022, Trichandi et al., 2022) are popular methods for  
61 imaging the near-surface. Seismic monitoring of dynamic processes may be achieved using omnipresent am-  
62 bient seismic noise, a natural source of illumination in the Earth (Curtis et al., 2006; Obermann et al., 2015;  
63 Nakata et al., 2019), and dense arrays of seismometers may be used to provide a repeatable data source  
64 with high spatial resolution. Ambient noise seismology has thus allowed velocity changes over time to be  
65 monitored in the critical zone (James et al., 2019; Oakley et al., 2021).

66

67 Seismic methods usually focus on the retrieval of seismic velocities only, and are unable to isolate the signal  
68 corresponding to subsurface density unambiguously. Density values are often inferred via empirical relation-  
69 ships from the speed of P body-waves (e.g. Gardner et al., 1974) or less commonly from S-wave speeds (e.g.,  
70 Miller and Stewart, 1991), and estimating density as a seismic observable still remains a challenge. Body  
71 wave travelttime tomography exhibits an inherent insensitivity to density changes: body wave scattering  
72 caused by a density contrast characteristically propagates backwards rather than forwards, and so to first  
73 order does not interact with the forward propagating incident wave whose travelttime is measured (Fichtner,  
74 2010). Surface waves, however, can be represented as an infinite sum of reflections and conversions between  
75 the free surface and subsurface interfaces, where the reflection coefficients depend on the density in the  
76 vicinity of the surface; this in turn affects the phase velocities of dispersive surface waves. Their frequency  
77 dependent arrival times are therefore sensitive to density variations in the subsurface, but the sensitivity is  
78 oscillatory with depth and can cancel destructively (Takeuchi and Saito, 1972).

79

80 In the context of global seismology, where density plays an important role in explaining mantle dynamics,  
81 several studies have been conducted to invert for density from surface wave data. Nolet et al. (1977) showed  
82 that Rayleigh wave dispersion data are sensitive to the density structure in elastic media, as are normal modes  
83 at longer periods (Tanimoto, 1991). It is however usually considered too challenging to estimate density in  
84 most elastic media using surface wave dispersion alone because the sensitivity is relatively weak compared  
85 to sensitivity to seismic velocity structure (Muyzert and Snieder, 2000). Due to the poor constraints on den-  
86 sity, it has been common practice in surface wave tomography to prescribe a scaling relation between density  
87 and shear velocity anomalies (Karato and Karki, 2001) and to invert for velocity only. From seismological  
88 research, however, we know that anti-correlation of density and seismic velocity are observed: Resovsky and

89 Trampert (2003) show that the long period seismic data clearly favour density perturbations that are poorly  
90 or negatively correlated with velocity heterogeneity and have larger amplitudes. The uniform scaling of  
91 velocity and density in tomography arises under the assumption that density variations are purely thermal;  
92 this is not accurate for density variations related to compositional heterogeneities or liquid/gas inclusions  
93 (Płonka et al., 2016). Therefore, independent knowledge of density is important in order to discriminate  
94 between compositional and thermal heterogeneities (Trampert et al., 2004; Mosca et al., 2012). Additional  
95 observables such as horizontal to vertical ratios (H/V) of surface waves can provide further constraints on  
96 density (Lin et al., 2012) but still show strong trade-offs with elastic parameters and velocity.

97

98 Variations in density also generally have a smaller effect on the full, recorded seismic waveforms than varia-  
99 tions in seismic velocity (Blom et al., 2017), and are subject to strong trade-offs with velocity which depend  
100 on the scattering angle of the wave (Luo and Wu, 2018). Nevertheless, Płonka et al. (2016) show that  
101 amplitude variations caused by realistic crustal density variations have measurable effects on seismograms.  
102 Density effects are mainly visible as an amplitude change, but also cause the waveform shape to be altered  
103 especially in the scattered wave train (Blom et al., 2017; Yuan et al., 2015). Hence, seismic methods that  
104 investigate the full seismic waveform such as full waveform tomography (Płonka et al., 2016; Blom et al.,  
105 2017; Blom et al., 2020) which includes both phases and amplitudes of body, surface and scattered waves,  
106 show promise to glean further constraints on subsurface density. However, in elastic multi-parameter full  
107 waveform inversion (FWI), the highest ambiguity is attached to density regardless of the employed model  
108 parametrizations (Köhn et al., 2012), and it is difficult to reconstruct density from full waveform inversion  
109 even using the dense data sets available in industrial exploration geophysics (Virieux and Operto, 2009).  
110 Choi et al. (2008) successfully estimated density from 2D elastic Marmousi models, but only using a low and  
111 narrow frequency band around 0.125 Hz. W. Pan et al. (2018) observed that S-wave velocity perturbations  
112 strongly contaminate density structure which can result in highly uncertain density estimates. Jeong et al.  
113 (2012) reports improvement in density recovery by implementing a 2-step algorithm that estimates Lamé  
114 parameters with fixed density in a first step, then velocity and density are estimated in a subsequent step  
115 that varies the number of free parameters in an iterative scheme. Subsurface density of the ocean floor can be  
116 reliably estimated from real hydrophone data on the basis of a joint visco-acoustic FWI (Prieux et al., 2013;  
117 Operto and Miniussi, 2018) and can be used as a background model to inform and reduce free parameters  
118 in elastic FWI. However, the performance of linearised FWI algorithms depends on a well informed starting  
119 model (Virieux and Operto, 2009; Vantassel et al., 2022).

120

121 Density affects the seismic wavefield mainly through reflection/backscattering. Hence, the strongest sensi-

122 tivity of seismic waves is to spatial density contrasts or gradients (Blom et al., 2020). Hooke's law relates  
123 stress to strain, and strain is created by spatial wavefield gradients. In turn, stress can be related to density  
124 using Newton's second law, to form a so-called wave equation. This sparked interest in constraining density  
125 contrasts by deploying methods that are directly sensitive to amplitude changes in the wavefield gradients.  
126 Dense seismic arrays lend themselves well to the calculation of wavefield gradients using finite-difference  
127 methods.

128

129 A class of imaging techniques now termed seismic gradiometry (Curtis and Robertsson, 2002; Langston,  
130 2007b; Langston, 2007c; De Ridder and Biondi, 2015) calculate temporal and spatial gradients of incoming  
131 waves or wavefields using dense array measurements to estimate physical subsurface parameters. A review  
132 of the theoretical background and applications of the wave gradiometry method can be found in Liang et al.  
133 (2023). One such method called wave equation inversion (WEI - Curtis and Robertsson, 2002) substitutes  
134 the calculated gradients directly into the governing equation for wave propagation and provides estimates of  
135 local material properties via standard linear inversion techniques. By deploying a 3D seismic array geom-  
136 etry with receivers recording all three components (3-C) of the wavefield, gradients can be estimated both  
137 horizontally at the surface and with respect to depth (Fig. 1a). WEI can then be performed on the full  
138 elastic wave equation to estimate effective P and S wave velocities at the free surface. In an isotropic, locally  
139 homogeneous Earth, full elastic WEI is valid for any incoming wavefield; it thus has the advantage of being  
140 directly applicable to ambient seismic wavefields, but exhibits a high sensitivity to receiver positioning and  
141 orientation (Muijs et al., 2002; Vossen et al., 2004). A second type of gradiometric research assumes a par-  
142 ticular form or ansatz for the arriving wavefield (e.g., a single plane or spherically spreading wave (Fig. 1b),  
143 and estimates parameters that describe the geometrical spreading and horizontal slowness (Langston, 2007a;  
144 Langston, 2007c). The method was applied for example as a new data processing technique for regional  
145 array seismology (Liang and Langston, 2009; Liu and Holt, 2015) and used to image the lunar near-surface  
146 structure (Sollberger et al., 2016). The method performs well for noiseless single source data, but gradiome-  
147 try results based on the plane-wave assumption are highly sensitive to uncorrelated noise and to interference  
148 from other arriving waves (Langston, 2007b). In order to use such methods in cases of unclassified wave type  
149 arrivals or ambient seismic noise, where two or more waves of similar amplitude and frequency are interfering,  
150 a statistical routine to identify individual interference-free events needs to be applied in advance (Edme and  
151 Yuan, 2016). A novel 'fingerprinting' technique based on 6C receiver measurements, which contain both  
152 translational and rotational ground motion, now allows to rapidly classify the wave types of seismic phases  
153 and extract individual arrivals from interfering wavefields using machine learning methods (Sollberger et al.,  
154 2023).

156 In the case of an ambient seismic noise field, it is commonly assumed that surface waves are the dominating  
 157 type of wave propagation. To capture the character of 2D surface wave propagation, it is sufficient to record  
 158 the wavefield with a dense receiver array at the Earth's surface (Fig. 1c). This relaxes the condition on the  
 159 field acquisition geometry compared to volumetric gradiometry which requires a 3D array (Fig. 1a), while still  
 160 allowing a wavefield comprising a superposition of plane waves arriving from different angles to be considered  
 161 instead of only individual plane waves (Fig. 1b). De Ridder and Biondi (2015) first approximated surface  
 162 wave WEI on the basis of the 2D Helmholtz wave equation which describes the propagation of surface waves  
 163 at frequency dependant phase velocities (Wielandt, 1993; Aki and Richards, 2002). The method showed that  
 164 phase velocity maps from the vertical component of ambient noise data at 0.7 Hz were comparable to results  
 165 from interferometric cross-correlations, thus validating the method. The method has since been extended  
 166 to provide information on both isotropic and anisotropic local medium properties (De Ridder and Curtis,  
 167 2017), and to near-real time applications (Cao et al., 2020).

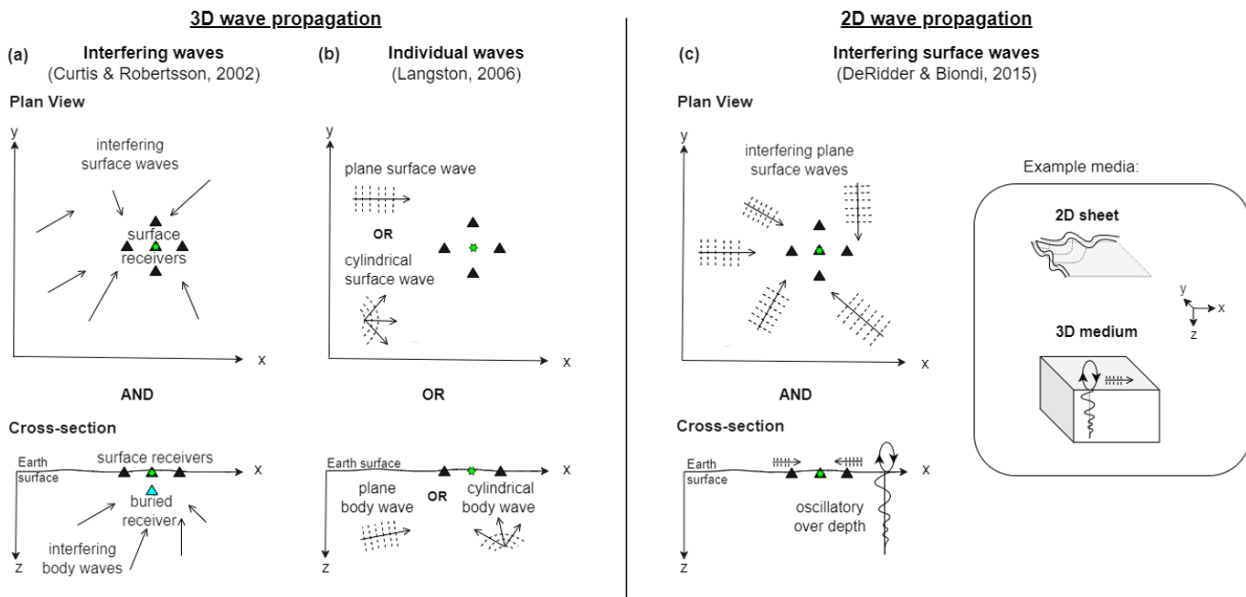


**Figure 1:** Schematic of acquisition geometries and physical assumptions made for different gradiometry types in plan view and cross-section view. Receivers are denoted by triangles and the configurations requiring the minimum number of receivers are shown to estimate gradients via classical finite difference around the central point (green star) with receivers recording translational motion. (a) The left column shows principles of volumetric wavefield gradiometry as proposed by (Curtis and Robertsson, 2002): with a 3D receiver acquisition, second horizontal and vertical wavefield derivatives are approximated at a central point. To calculate derivatives in x-, y- and z-direction, 3-component (3C) receivers are necessary. Arrows denote interfering waves coming from all directions and angles; all wave types can be included in the wavefield e.g., surface waves, body waves, scattered waves, etc. (b) Middle column shows gradiometry for non-interfering waves as proposed by (Langston, 2007b). Individual plane or cylindrical waves can arrive from any direction at the receiver array. Receivers are used to estimate first horizontal derivatives of the wave field quantity; the central point does not require a recording. Receivers can be (1C) or (3C) depending on which wave type is analysed. Rotational sensors at the free surface allow for direct measurement of first derivatives (Schmelzbach et al., 2018; Sollberger et al., 2020). (c) Right column shows principles of surface wave gradiometry as proposed by (De Ridder and Biondi, 2015) where second order horizontal wavefield derivatives are approximated. This gradiometry type assumes a wavefield composed of interfering surface plane waves in a 3D medium, or Lamb waves in a 2D sheet (inset).

168 The latter applications of surface wave WEI are based on the assumption that Rayleigh waves are the domi-  
169 nant wave type and that the 2D scalar Helmholtz wave equation describes the recorded wavefield adequately  
170 (De Ridder and Biondi, 2015; Cao et al., 2020). This is a significant approximation for seismic waves because  
171 the Helmholtz equation fails to describe general elastic wavefield dynamics. Since ambient noise recordings  
172 contain all kinds of interfering elastic wave types (such as surface waves themselves), the accuracy of subsur-  
173 face material property estimates may be compromised. Nevertheless, Shaiban et al. (2022) used a synthetic  
174 2D elastic ambient noise wavefield to show that the correct local dispersion curves for a layered, laterally  
175 heterogeneous model could be estimated from the relationship between spatial and temporal gradients in  
176 the Helmholtz equation.

177

178 Surface wave WEI has been shown to require only a few minutes of ambient seismic noise recordings and  
179 rapid data processing after acquisition to produce useful phase velocity maps for the near-surface (at fre-  
180 quencies between 18 Hz to 24 Hz), and so shows promise for efficient field deployment and near-real time  
181 monitoring purposes for the shallow subsurface (Cao et al., 2020). By estimating phase velocity maps for  
182 narrow band-pass filtered wavefields over a broad frequency range (depending on the ambient noise spec-  
183 trum), the latter authors showed that 3D images of a layered subsurface can be produced via inversion of  
184 local surface-wave dispersion curves for S-wave velocity ( $V_s$ ) structure. 2D shear-velocity maps for several  
185 depth levels up to 50 m were obtained in a matter of seconds from the dispersion curve through depth inver-  
186 sion performed by mixture-density neural networks (MDN). However, the quality of the 3D shear velocity  
187 models are not only dependant on the accuracy of the phase velocity data but also on the impact of density  
188 in the inversion process (Ivanov et al., 2016). Dispersion-curve inversion for  $V_s$  generally uses predefined  
189 values for compressional-wave velocity ( $V_p$ ) and density because their sensitivities to the phase velocity are  
190 much smaller than that of the S-wave velocity (Foti et al., 2018; L. Pan et al., 2019; Wu et al., 2020). Such  
191 a-priori information on  $V_p$  is commonly obtained from other measurements and density is often assumed  
192 constant (e.g. Cao et al., 2020) or inferred from empirical relationships with compressional wave speed.  
193 Unfortunately, vertical density variations have been shown to affect the inverted  $V_s$  results, and the use of  
194 an inaccurate density background model can lead to false structures and overestimations in the  $V_s$  result  
195 (Ivanov et al., 2016). Expanding surface wave WEI to estimate the density structure of the subsurface and  
196 to quantify the effect of density gradients on the phase velocity estimates could therefore improve  $V_s$  models  
197 and seismic interpretation based on gradiometric methods.

198

199 In this study we investigate whether it is possible to estimate subsurface density on the basis of gradiometric  
200 surface wave WEI using ambient seismic noise. Both the accuracy in wave amplitude and shape are impor-

tant considerations in gradiometric methods, and density heterogeneities were found to have an influence on both (Płonka et al., 2016; Blom et al., 2017). Hence, we expect to have sensitivity to the effect of density contrasts by using data that record variations in wavefield amplitudes and phases.

204

In the Helmholtz formulation, which has been used in previous surface wave WEI studies, the wave equation does not exhibit an explicit sensitivity to density. In elastic media, the scalar Helmholtz wave equation is valid for surface waves only in laterally homogeneous medium. In a realistic scenario, the subsurface is heterogeneous with velocity and density varying both laterally and with depth. In heterogeneous media, the superposition of multipathing surface waves propagates with a velocity that does not only depend on the structural properties of the underlying medium, but also on the distribution of amplitudes of the interfering wavefield (Friederich et al., 2000). This implies that the Helmholtz wave equation is not a valid description for surface wave propagation and is likely to influence the accuracy of phase velocity estimates made via 2D scalar WEI. In practice, if the medium is only smoothly heterogeneous, the Helmholtz equation is usually considered to be approximately valid for each surface wave mode separately. Seismic surface waves are however commonly approximated by acoustic waves, by assuming that the wavefield is purely dilatational and is dominated by pressure wave propagation. The acoustic approximations neglects mode conversions and the directivity of scattering from a point heterogeneity (Friederich et al., 2000), simplifying the mathematical model of wave propagation considerably.

219

The scalar Helmholtz wave equation more accurately describes waves in acoustic media than in elastic media. In fact in the acoustic case, the main simplification made in the derivation of the conventional scalar wave equation is that density is assumed to be constant across the local receiver array. To describe a more complex, physically more realistic medium, a variable density assumption can be made, which allows the acoustic medium to be described by a so-called full acoustic wave equation. The full acoustic wave equation was initially derived by Bergmann (1946) to define conditions under which density gradients in the atmosphere and large bodies of water should not be neglected in the governing wave equation formulation of sound pressure. The formulation of the full acoustic wave equation considered in that work assumes that gravity effects are negligible, and allows for density changes caused by either temperature gradients or changes in chemical composition of the material (Bergmann, 1946).

230

In this paper we analyse wavefield sensitivities to subsurface density contrasts via WEI of the full-acoustic wave equation where density is treated as a variable. We expect the full acoustic formulation may allow us to analyse the role of density independently from wave speed. To test this hypothesis, we initially consider

234 waves propagating through an acoustic medium so that the physics of the used wave equation are consistent  
 235 with the physics of the medium. We show that it is possible to invert for density on the basis of full acoustic  
 236 WEI and compare the effect of using the Helmholtz and full acoustic equation on phase velocity results in  
 237 3D acoustic media. We then analyse whether the procedure is applicable to elastic media despite the con-  
 238 comitant severe approximations to the complex elastic wavefield physics. In elastic media, particle velocity  
 239 is the natural wavefield observable rather than pressure, but we show that measuring pressure is necessary in  
 240 order to relate the full acoustic wave equation approximation to the elastic case and to formulate an inverse  
 241 algorithm that is explicitly sensitive to density. We then investigate whether volumetric gradiometry better  
 242 lends itself to invert for density using the physically more representative full elastic wave equation at the  
 243 free surface. By expressing the full elastic wave equation both in terms of pressure and displacement at the  
 244 free surface we establish that a direct sensitivity to density exists and that density can be estimated.

245

## 246 **2 Wave Theoretical Background**

247 Density plays a different role in elastic and acoustic media. To illustrate, we compare the derivations of the  
 248 respective governing wave equations from Newton's 2<sup>nd</sup> Law

$$\nabla \cdot \sigma + \mathbf{f} = \rho \partial_t^2 \mathbf{u} \quad (1)$$

249 where  $\sigma = \sigma_{kl}$  is the stress tensor assuming k and l to range from 1 to 3 (for the x, y and z directions),  $\rho$  is  
 250 subsurface density,  $\mathbf{f} = [f_x, f_y, f_z]^T$  is the distribution of applied body forces,  $\mathbf{u} = [u_x, u_y, u_z]^T$  the observed  
 251 wave field quantity of displacement or particle velocity, and  $\nabla = [\partial_x, \partial_y, \partial_z]^T$  in three dimensional media.  
 252 The wave field quantity  $\mathbf{u}$  is defined with respect to a reference state in which the medium is in equilibrium  
 253 under gravity. It is well known that in isotropic elastic media and small displacements, Hooke's law allows  
 254 stress to be expressed in terms of the strain tensor  $\varepsilon$  (where element  $\varepsilon_{xy} = \partial_x u_y + \partial_y u_x$  and similarly for  
 255 other elements) and the Lamé parameters  $\lambda$  and  $\mu$ . This relationship can then be substituted in equation  
 256 (1). Similarly for acoustic media, however the equations are then simpler because the shear modulus  $\mu = 0$ :

$$\nabla \cdot (\lambda \text{tr}(\varepsilon) \mathbf{I} + 2\mu \varepsilon) + \mathbf{f} = \rho \partial_t^2 \mathbf{u} \quad \text{in elastic media} \quad (2a)$$

$$\nabla \cdot (\lambda \text{tr}(\varepsilon) \mathbf{I}) + \mathbf{f} = \rho \partial_t^2 \mathbf{u} \quad \text{in acoustic media} \quad (2b)$$

257 where  $\text{tr}()$  is the trace operator. By substituting expressions for elements of  $\varepsilon$  into equations (2a) and (2b)  
 258 we obtain the familiar 3D elastic wave equation for isotropic, locally homogeneous media, and a description  
 259 of pressure wave propagation in terms of the wave field quantity  $\mathbf{u}$ , respectively:

$$\frac{(\lambda + 2\mu)}{\rho} [\nabla(\nabla \cdot \mathbf{u})] - \frac{\mu}{\rho} [\nabla \times (\nabla \times \mathbf{u})] + \frac{\mathbf{f}}{\rho} = \partial_t^2 \mathbf{u} \quad \text{in elastic media} \quad (3a)$$

$$\frac{\lambda}{\rho} [\nabla(\nabla \cdot \mathbf{u})] + \frac{\mathbf{f}}{\rho} = \partial_t^2 \mathbf{u} \quad \text{in acoustic media} \quad (3b)$$

260 In this paper we focus on the case in which we would like to use ambient seismic noise, so we assume an  
 261 absence of strong local sources in the area of wavefield recording and henceforth omit source term  $\mathbf{f}$ . In  
 262 acoustic media, the first Lamé parameter  $\lambda$  is the acoustic bulk modulus  $K_a$ , whereas the bulk modulus  
 263 in elastic media is  $K_e = \lambda + \frac{2}{3}\mu$ . In elastic media, density is expressed only in combination with the  
 264 Lamé parameters within the terms equating to P-wave velocity  $v_{P,e} = \sqrt{(\lambda + 2\mu)/\rho}$  and S-wave velocity  
 265  $v_{S,e} = \sqrt{\mu/\rho}$  respectively in equation (3a), and similarly for acoustic media. This implies that while it may  
 266 be possible to estimate the velocities from waveform data  $\mathbf{u}$ , it will not be possible to discriminate the Lamé  
 267 parameters from the density since any velocity value can be fit by any density given a suitable choice of  $\lambda$   
 268 and  $\mu$ .

269

270 In acoustic media, we often measure pressure  $P$  rather than wavefield displacement or particle velocity. The  
 271 particle velocity field can then be estimated from this measured pressure field (Robertsson and Kragh, 2002;  
 272 Amundsen et al., 2005). Pressure is directly related to the divergence of the wavefield displacement  $\mathbf{u}$  via the  
 273 equality  $P = K_a \nabla \cdot \mathbf{u}$ , where  $K_a$  is the bulk modulus in acoustic media. By applying a divergence operator to  
 274 both sides of the acoustic wave equation (3b) it is possible to express an explicit sensitivity of measurements  
 275 of pressure  $P$  to density  $\rho$ :

$$\nabla \cdot \left( \frac{K_a}{\rho} [\nabla(\nabla \cdot \mathbf{u})] \right) = \nabla \cdot \partial_t^2 \mathbf{u} \quad (4)$$

$$\Rightarrow v_{P,a}^2 \rho \nabla \cdot \left( \frac{1}{\rho} \nabla P \right) = \partial_t^2 P \quad (5)$$

276 where in equation (5) we have used the definition of P wave velocity in acoustic media  $v_{P,a} = \sqrt{K_a/\rho}$ .  
 277 Since density appears separately from P-wave velocity and has a different relationship to the measurable  
 278 right hand side of equation (5), we expect a potentially distinguishable density signature in seismic waves  
 279 travelling through heterogeneous media in which the spatial derivative of density on the left is non-zero.

280

281 Cance and Capdeville (2015) show how elastic and acoustic wave equations can be related in an isotropic,  
 282 homogeneous domain for an explosive isotropic source emitting only P-waves. In such a case, the curl of  
 283 the wavefield is equal to zero ( $\nabla \times \mathbf{u} = 0$ ) and any vector field such as the displacement  $\mathbf{u}$  or the particle  
 284 velocity field  $\mathbf{v} = \partial_t \mathbf{u}$  can be derived from a potential  $\Phi$  (Kaufman et al., 2000). The potential  $\Phi$  may be  
 285 chosen as in Cance and Capdeville (2015) to be

$$\mathbf{u} = \frac{1}{\rho} \nabla \Phi \quad (6)$$

286 where  $\Phi$  is directly related to acoustic pressure via the relationship  $\Phi = -2P_e$  and where the pressure  
 287 wavefield  $P_e$  in elastic media is

$$P_e = -\frac{1}{2} K_a \nabla \cdot \mathbf{u} \quad (7)$$

288 Substituting equation (6) into equation (3a) yields,

$$\frac{\lambda + 2\mu}{\rho} \nabla \left[ \nabla \cdot \left( \frac{1}{\rho} \nabla \Phi \right) - \frac{1}{\lambda + 2\mu} \partial_t^2 \Phi \right] = 0 \quad (8)$$

$$\nabla \cdot \left( \frac{1}{\rho} \nabla \Phi \right) - \frac{1}{\lambda + 2\mu} \partial_t^2 \Phi = \text{const} \quad (9)$$

289 Since equation (8) holds everywhere and so the constant is independent of position of the recording, and  
 290 because the wave is absent (has zero energy) at infinity (Kaufman et al., 2000), equation (9) gives the  
 291 potential equation in elastic media,

$$c_\omega^2 \rho \nabla \cdot \left( \frac{1}{\rho} \nabla \Phi \right) = \partial_t^2 \Phi \quad (10)$$

292 where  $c_\omega$  is the phase velocity at frequency  $\omega$ . Equation (10) describes acoustic wave propagation in elastic  
 293 media and is the elastic equivalent of equation (5) for acoustic media.

294

295 The above equations show that different seismic observables interact differently with the subsurface: to iso-  
 296 late the effect of density from wave speed in elastic media on the basis of the full acoustic approximation  
 297 or the elastic wave equation at the free surface, it is necessary to measure pressure instead of particle dis-  
 298 placement or velocity (equations 6 to 10) because pressure implicitly includes a power of  $K_a$  which changes  
 299 the form of the respective equations. Classical seismometers only measure particle velocity, from which  
 300 displacement can be calculated by time integrating the data, whereas elastic pressure is usually not observed

301 on land. The expression for pressure is proportional to the divergence of the displacement (eq. 7) which can  
 302 be determined from four geophone recordings at the Earth's free surface using gradiometry (Robertsson and  
 303 Muyzert, 1999; Shapiro et al., 2000; Robertsson and Curtis, 2002). Given that stress is equal to zero across  
 304 the free surface, the vertical derivative of the wavefield can be expressed in terms of horizontal derivatives.  
 305 This results in the wavefield divergence taking a modified form that can be written in terms of the Lamé  
 306 parameters and the horizontal wavefield components only  $\nabla \cdot \mathbf{u} = (2\mu/(\lambda+2\mu)) \nabla_H \cdot \mathbf{u}_H$  where  $\nabla_H = [\partial_x, \partial_y]^T$   
 307 and  $\mathbf{u}_H = [u_x, u_y]^T$  (e.g. Maeda et al., 2016). However, calculating the divergence alone is not sufficient to  
 308 estimate subsurface density as the density signal is contained in the full pressure measurement (eq. 7).

309

310 Edme et al. (2018) suggest that it is possible to measure pressure directly at the free surface of an elastic  
 311 medium with a land hydrophone. The land hydrophone is insensitive to the direction and angle of incoming  
 312 waves which makes it predominantly sensitive to pressure fluctuations induced by ground-roll (more specif-  
 313 ically, S-to P-conversions generated by upcoming S-waves) due to destructive summation of events at near  
 314 vertical incidence angle. At the free surface of the Earth, elastic pressure  $P_{e,FS}$  can be written in terms of  
 315 displacement in a 2D plane and its horizontal derivatives as (Edme et al., 2018)

$$P_{e,FS} = K_{e,FS} \nabla_H \cdot \mathbf{u}_H \approx 0.37 K_a \nabla_H \cdot \mathbf{u}_H \quad (11)$$

316 where the elastic bulk modulus at the free surface is  $K_{e,FS} = 2\varphi v_S^2 (1 - 4 v_S^2 / 3 v_P^2)$  and  $v_P$  and  $v_S$  are the  
 317 local P- and S-wave velocities, respectively. The elastic pressure at the free surface can be related to acoustic  
 318 pressure using  $v_P = \sqrt{3}v_S$  for a Poisson solid. The measured pressure thus corresponds to the volume change  
 319 caused by the dilatational part of surface wave propagation.

320

321 Acoustic pressure caused purely by P-wave propagation in a non-rotational medium has a similar expression  
 322 to elastic pressure at the free surface caused by the dilatational part of surface wave propagation. Surface  
 323 waves can only be produced in a medium where rotation exists, and are generated by P- and S- wave in-  
 324 teractions upon reflections and scattering at medium heterogeneities. Their propagation is mostly driven  
 325 by S-waves which correspond to the purely rotational part of the wavefield. Nevertheless, Rayleigh waves  
 326 do exhibit dilatational wave propagation that produces a measurable pressure field at the free surface. The  
 327 full acoustic approximation is only valid for elastic P-waves in a homogeneous, isotropic medium, and is  
 328 compromised in heterogeneous or anisotropic media due to P-to-S conversions. It thus does not describe a  
 329 wave type that depends on body-wave conversions that are predominantly controlled by S-wave motion, even  
 330 if only its compressional part is recorded. P-waves and the P component of Rayleigh waves therefore pre-

331 sumably interact differently with the medium and might exhibit different sensitivities to different subsurface  
 332 parameters such as subsurface density. Cance and Capdeville (2015) found that acoustic and elastic pressure  
 333 are not the same for rough, heterogeneous media: a good agreement can only be achieved in homogeneous  
 334 or weakly heterogeneous, smooth media. This suggests that in a realistic subsurface problem, inverting for  
 335 the parameters on the basis of an acoustic approximation might be too approximate an approach to obtain  
 336 sufficiently accurate information about elastic subsurface parameters by measuring pressure. We test this in  
 337 what follows.

338

339 In elastic media it is not strictly necessary to consider the acoustic approximation in order to isolate density  
 340 by substituting pressure. If we introduce the free surface conditions

$$\partial_z u_x = -\partial_x u_z \quad (12)$$

$$\partial_z u_y = -\partial_y u_z \quad (13)$$

$$\partial_z u_z = -\frac{v_{P,e}^2 - 2v_{S,e}^2}{v_{P,e}^2} (\partial_x u_x + \partial_y u_y) \quad (14)$$

341 which express the fact that stress across the free surface must be zero, then equation (3a) can be written in  
 342 a modified form that is valid at the free surface and in the absence of body forces:

$$\partial_z^2 u_x = \frac{\partial_t^2 u_x}{v_{S,e}^2} - (\nabla_H^2 u_x) - 2\left(1 - \frac{v_{S,e}^2}{v_{P,e}^2}\right) \partial_x (\nabla_H \cdot \mathbf{u}_H) \quad (15)$$

$$\partial_z^2 u_y = \frac{\partial_t^2 u_y}{v_{S,e}^2} - (\nabla_H^2 u_y) - 2\left(1 - \frac{v_{S,e}^2}{v_{P,e}^2}\right) \partial_y (\nabla_H \cdot \mathbf{u}_H) \quad (16)$$

$$\partial_z^2 u_z = \frac{\partial_t^2 u_z}{v_{P,e}^2} + \left(1 - 2\frac{v_{S,e}^2}{v_{P,e}^2}\right) \nabla_H^2 u_z \quad (17)$$

343 Even though a free-surface is usually referred to as the interface of a half-infinite elastic medium in contact  
 344 with vacuum (Robertsson et al., 1995), free-surface conditions are a reasonable approximation on Earth  
 345 given that the subsurface has elastic properties and the contact layer is air, which has low density. In the  
 346 case of granular medium (such as regolith) or in heavy atmospheres, the free-surface condition would need  
 347 to be updated with more appropriate constraints.

348

349 By using a so-called Lax-Wendroff derivative centering technique (Lax and Wendroff, 1964; Blanch and  
 350 Robertsson, 1997; Curtis and Robertsson, 2002), the first order vertical derivative can be correctly repre-  
 351 sented at the free surface by a finite difference approximation to horizontal spatial derivatives. Using a 3D

352 receiver array as proposed in Fig. 1(a) it then becomes possible to approximate all quantities necessary to  
 353 estimate body wave velocities at the free surface. For example, a new expression can be derived for the  
 354 vertical displacement component in eq. (17) by using the free-surface condition (14) and the Lax-Wendroff  
 355 corrected finite difference depth derivative:

$$\partial_t^2 u_z = v_{P,e}^2 A_z(t) - v_{S,e}^2 B_z(t) \quad (18)$$

356 where  $A_z(t)$  and  $B_z(t)$  are expressions containing finite difference approximations to derivatives of the wave-  
 357 field

$$A_z(t) = \frac{2}{\Delta z} (\nabla_H \cdot \mathbf{u}_H + [\partial_z u_z]_{fd}) - \nabla_H^2 u_z \quad (19)$$

$$B_z(t) = \frac{4}{\Delta z} (\nabla_H \cdot \mathbf{u}_H) - 2(\nabla_H^2 u_z) \quad (20)$$

358 and where  $\Delta z$  is the distance between the surface and the buried receiver, and  $[\partial_z u_z]_{fd}$  is the first order finite  
 359 difference depth derivative. The derivation of these expressions is described in detail in Curtis and Roberts-  
 360 son (2002), and herein, we only consider the constraints derived from the vertical displacement component  
 361 as they were shown to better constrain body wave velocity estimates than those derived from horizontal  
 362 components. Furthermore, inhomogeneous terms do not play a role in the vertical component at the free  
 363 surface, making the expressions valid for any type of elastic medium without approximations (Appendix E).

364

365 By using the relation  $P = P_{e,FS}/0.37$  from eq. (11), acoustic pressure can be substituted into eq. (19) and  
 366 (20):

$$A'_z(t) = \frac{2}{\Delta z} \left( \frac{1}{K_a} P + [\partial_z u_z]_{fd} \right) - \nabla_H^2 u_z \quad (21)$$

$$B'_z(t) = \frac{4}{\Delta z} \frac{1}{K_a} P - 2(\nabla_H^2 u_z) \quad (22)$$

367 Feeding the expressions for  $A'_z(t)$  and  $B'_z(t)$  into eq. (18) we obtain

$$\partial_t^2 u_z + v_{P,e}^2 \left[ -\frac{2}{\Delta z} [\partial_z u_z]_{fd} + \nabla_H^2 u_z \right] - 2v_{S,e}^2 \nabla_H^2 u_z = \frac{1}{\rho} \left[ \frac{1}{\Delta z} \left( 2 - \frac{4v_{S,e}^2}{v_{P,e}^2} \right) P \right] \quad (23)$$

368 Displacement measurements are all on the left-hand side and pressure measurements on the right-hand side  
 369 of equation (23); in order to use this equation to constrain the velocities and density, both displacement and  
 370 pressure must be measured simultaneously at the free surface. An explicit sensitivity becomes clear from eq.

371 (23) with density connecting the left- and right-hand sides of the equation linearly.

372

### 373 3 Gradiometric Methodology

374 Herein, we focus on the potential of gradiometric methods based on 2D surface arrays (e.g., De Ridder  
375 and Biondi (2015) in Figure 1c) and 3D volumetric arrays (e.g., Curtis and Robertsson (2002) in Figure  
376 1a) to estimate density in addition to medium speed. We start outlining the 2D gradiometric methodology  
377 (Section 3.1) for density inversion in light of equations (5) and (10). These equations are naturally suitable for  
378 acoustic wave propagation, but subject to drastic approximations in elastic media. We investigate whether a  
379 practical 2D array setup, that limits the complexity of the wave equation (vertical wavefield gradients can not  
380 be determined) employed for WEI, yields sufficient information to estimate density in an acoustic medium  
381 where the physics fit the employed equations (5) and (10), and extend the method to elastic media. We then  
382 test whether using a 3D array configuration (Section 3.2) with an additional buried receiver, which makes  
383 it possible to use a physically more appropriate equation for elastic data (i.e., equation 23), improves the  
384 density estimates in elastic media. The following sections are hence structured according to the gradiometric  
385 WEI approaches for density estimation based on free surface (Section 3.1) and volumetric array recordings  
386 (Section 3.2), respectively.

#### 387 3.1 Free surface arrays

388 In previous wavefield gradiometry studies performed with data from 2D receiver arrays on the Earth's surface,  
389 the role of density has been neglected. If density is assumed to be constant over space, equation (10) reduces  
390 to the scalar Helmholtz wave equation, the 2D version of which is usually used as a basis for WEI where  $\nabla$   
391 is used as a 2D operator ( $\nabla = \nabla_H = [\partial_x, \partial_y]^T$ ) and  $\mathbf{x} = [x, y]^T$ :

$$c_\omega(\mathbf{x})^2 \nabla^2 \vartheta(\mathbf{x}, t) = \partial_t^2 \vartheta(\mathbf{x}, t) \quad (24)$$

392 Here,  $\vartheta$  denotes any type of wavefield quantity (e.g., one component of the wavefield displacement or particle  
393 velocity field, or the pressure field) which varies as a function of horizontal position  $x$  and  $y$  and time  $t$ .  
394 This equation is a significant approximation to how seismic waves propagate in the Earth's subsurface: all  
395 3D propagation of elastic body waves and of different types of surface wave, each associated with multi-  
396 component particle motions, are approximated by a single wave type propagating in 2D across the Earth's  
397 surface with a single independent component of particle motion. For example, in isotropic media Love waves

398 are horizontally polarized and arrive most prominently on the transverse component, whereas the Rayleigh  
 399 waves are polarized in a vertical plane and appear mainly on the vertical and radial components (Shearer,  
 400 2019). In the case of ambient noise, we deal with complex wavefields arriving from multiple sources which  
 401 makes it impossible to distinguish radial contributions from transverse contributions; Love and Rayleigh  
 402 waves therefore interfere in the horizontal particle velocity field yet are treated as one wave type in the 2D  
 403 scalar wave equation. On land, 1C geophone recordings are usually employed as gradiometric measurements,  
 404 because Rayleigh waves typically dominate the ambient seismic noise field and predominantly excite vertical  
 405 displacements. A similar argument applies to Scholte waves which travel along the water-seabed interface.  
 406 And since surface waves predominantly travel across the Earth's surface and have a dominant mode number,  
 407 they are commonly approximated by superpositions of dispersive, single-mode plane waves that each satisfy  
 408 the 2D scalar wave equation.

409

410 In order to improve the suitability of the Helmholtz approximation for surface waves, the wavefield is usually  
 411 first filtered around a fixed frequency  $\omega$ . WEI then proceeds by estimating all spatial and temporal deriva-  
 412 tives in equation (24) given measurements of a passing wavefield made on a dense array. Thereafter the  
 413 equation can be solved for the phase velocity  $c_\omega$ . Nevertheless, the series of approximations above degrades  
 414 the estimates of surface wave velocity.

415

416 In acoustic media however, the Helmholtz wave equation may be a reasonable model of wave propagation  
 417 because the only approximation made in governing physics is that density is assumed to be locally constant  
 418 across the array of receivers used to estimate spatial derivatives in  $\nabla P$ . To account for a spatial variability  
 419 in subsurface density, we consider the full acoustic wave equation in the time domain:

$$\nabla \cdot \left( \frac{1}{\rho(\mathbf{x})} \nabla P(\mathbf{x}, t) \right) = \frac{1}{\rho(\mathbf{x}) c_\omega(\mathbf{x})^2} \partial_t^2 P(\mathbf{x}, t) \quad (25)$$

420 The full acoustic wave equation represents the underlying physics that relates phase velocity  $c_\omega$  and density  
 421  $\rho$  to dilatational wavefield observations where pressure  $P$  is used as wavefield quantity  $\Phi$ . In acoustic media,  
 422 equation (25) captures the full physics whereas it is only an approximation of wave propagation in elastic  
 423 media. To perform WEI on the basis of the full acoustic wave equation in elastic media, we need to compute  
 424 the pressure wavefield  $P$  from equation (7) and substitute the resulting potential  $\Phi = K_a \nabla \cdot \mathbf{u}$  into equation  
 425 (10) where  $\mathbf{u} = \mathbf{u}_H$  and  $\nabla = \nabla_H$ .

426

427 Using the foundation of the full acoustic wave equation we set up an inversion process to estimate both  
 428 velocity and density from gradiometric measurements. We first parametrize the system in order to remove  
 429 non-linearity in these forward relations. We simplify the form of equation (25) by introducing parameters  
 430  $g(\mathbf{x})$  and  $h(\mathbf{x})$  that vary as a function of horizontal position:

431

$$h(\mathbf{x}) = \frac{1}{K(\mathbf{x})} = \frac{1}{\rho(\mathbf{x})c_\omega(\mathbf{x})^2} \quad (26)$$

$$g(\mathbf{x}) = \frac{1}{\rho(\mathbf{x})} \quad (27)$$

432 The full acoustic wave equation then becomes

$$\nabla g(\mathbf{x}) \nabla P(\mathbf{x}, t) = h(\mathbf{x}) \partial_t^2 P(\mathbf{x}, t) \quad (28)$$

433 We rely on accurate knowledge of second order spatial gradients of pressure which can not be measured  
 434 directly in the field. We calculate these gradients discretely using finite differences which are based around  
 435 Taylor series expansions (Curtis and Robertsson, 2002). We discretize equation (28) on a horizontal, regularly  
 436 spaced receiver grid at the surface (Fig. 2a) using classical central finite differences (FD) after (Geiger and  
 437 Daley, 2003) to approximate the derivatives. Discretizing with the FD method does not require regular  
 438 grids if we adopt a generalized FD scheme after (Liszka and Orkisz, 1980; Huiskamp, 1991; Gavete et al.,  
 439 2003), however in our case receiver spacing  $\Delta x$  and  $\Delta y$  in x and y directions respectively are constant and  
 440 equal, and indices i and j define receiver locations where i ranges from [0,M] and j ranges from [0,N]. We  
 441 formulate the discretized expression and rearrange the terms isolating the model parameter  $g_{i,j}$  that contains  
 442 information about subsurface density only:

$$\frac{1}{2\Delta x^2} \left[ P_{[0,-]}^n g_{[i,j-1]} + P_{[-,0]}^n g_{[i-1,j]} \right. \\ \left. + P_{[\pm,\pm]}^n g_{[i,j]} + P_{[+,0]}^n g_{[i+1,j]} + P_{[0,+]}^n g_{[i,j+1]} \right] = h_{[i,j]} \left[ \frac{P_{[i,j]}^{n+1} - 2P_{[i,j]}^n + P_{[i,j]}^{n-1}}{\Delta t^2} \right] \quad (29)$$

443 where  $P_{[0,-]}^n$  and  $P_{[-,0]}^n$  are written similarly to

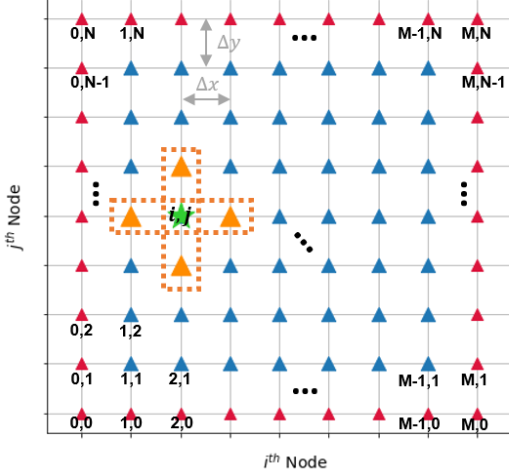
$$P_{[0,+]}^n = P_{[i,j+1]}^n - P_{[i,j]}^n \quad (30)$$

$$P_{[+,0]}^n = P_{[i+1,j]}^n - P_{[i,j]}^n \quad (31)$$

444 and

$$P_{[\pm,\pm]}^n = P_{[0,-]}^n + P_{[-,0]}^n + P_{[0,+]}^n + P_{[+,0]}^n \quad (32)$$

(a)



(b)

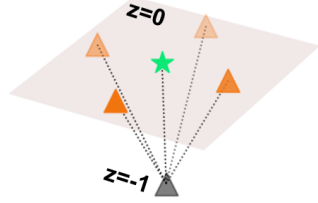


**Figure 2:** (a) Discretization of wavefield derivatives using a surface receiver grid, shown in plan view on the x-y plane. Receivers are marked by triangles (internal stations in blue, border stations in red). The grid has N rows in y-direction and M columns in x-direction. The pressure field P is recorded at each receiver position [i,j]. The classical second order finite difference stencil of receivers is represented by the cross-shape (orange), using which the second order derivative of the wavefield is estimated at the central point marked by the star symbol (green). (b) shows the corresponding buried receiver (grey) at 1m below the surface that is used for volumetric gradiometry across the finite difference cross-shaped stencil.

445 Equation (29) can be written in matrix form

$$\mathbf{A} \mathbf{g}^{\text{est}} = \mathbf{d} \quad (33)$$

446 where matrix  $\mathbf{A}$  has dimensions  $[R \times R \times n_t]$  with R being the number of parameters over the receiver grid  
 447 ( $R = M \times N$ ) and  $n_t$  the number of data in the time series.  $\mathbf{A}$  contains purely observed data consisting  
 448 of the pressure differences (equations 30 to 32) and is banded and square  $[R \times R]$  for each time step n in  
 449 the time series of the signal. Vector  $\mathbf{g}^{\text{est}} = [g_{[0,0]}, g_{[1,0]}, \dots, g_{[M,N]}]^T$  is the parameter vector of dimension  
 450  $[R \times 1]$  to be estimated, and  $\mathbf{d}$  is an observed data vector of dimension  $[R \times n_t]$  that contains time derivatives  
 451 of the recorded pressure field  $P_{i,j}$  multiplied by terms  $h_{i,j}$  (right-hand side of eq. 29). Equally accurate  
 452 calculations of derivatives at the corners and boundaries of the array are not possible since neighbouring  
 453 receivers are not available in all directions so the full cross-shaped finite difference stencil (Fig. 2) can not  
 454 be used and is depleted to a stencil formed by two or three adjacent stations only. We therefore introduce a

455 weighting matrix  $\mathbf{W}$  that gives less weight to information from corner and boundary points of the receiver  
 456 grid which are likely to provide less accurate constraints than the internal receivers. For corner and border  
 457 receivers we chose a weighting factor very close to zero to minimize the impact on results while still main-  
 458 taining the invertibility of matrix  $\mathbf{A}$ . Consequently, density estimates are evaluated only at internal receivers.  
 459

460 Since the density information is contained in both parameter vector  $\mathbf{g}^{\text{est}}$  and the vector  $\mathbf{d}$  through parameter  
 461 vector  $\mathbf{h} = [h_{[0,0]}, h_{[1,0]}, \dots, h_{[M,N]}]^T$ , prior information is given in the form of an initial reference model for  
 462  $\mathbf{h}$  which we call  $\mathbf{h}^{\text{init}}$ :

$$\mathbf{h}^{\text{init}} = \frac{1}{\rho_{\text{init}} c_{\omega,\text{init}}} \quad (34)$$

463 So as not to bias the inversion towards a heterogeneous solution, we chose a homogeneous reference for density  
 464  $\rho_{\text{init}}$ . The reference model  $c_{\omega,\text{init}}$  for phase velocity is obtained from an initial wave equation inversion using  
 465 the standard scalar Helmholtz wave equation formulation (24) following the methods of De Ridder and  
 466 Biondi (2015) and Cao et al. (2020). To stabilise the inverse problem we introduce generalized Tikhonov  
 467 regularization:

$$[\mathbf{WA} + \Theta_d \mathbf{I}] \mathbf{g}^{\text{est}} = [\mathbf{d} + \Theta_d \mathbf{g}^{\text{init}}] \quad (35)$$

468 Damping term  $\Theta_d$  controls how strongly the solution is drawn towards the homogeneous reference model  
 469  $\mathbf{g}^{\text{init}}$  and has the same dimensions as matrix  $\mathbf{A}$ . We then find the least-squares solution for parameters  $\mathbf{g}^{\text{est}}$   
 470 that contain the density information

$$\mathbf{g}^{\text{est}} = [\Sigma_{n=1}^{n_t} (\hat{\mathbf{A}}_n^T \hat{\mathbf{A}}_n)^{-1} \hat{\mathbf{A}}_n^T] [\Sigma_{n=1}^{n_t} \hat{\mathbf{d}}_n] \quad (36)$$

471 where  $\hat{\mathbf{A}} = [\mathbf{WA}, \Theta_d \mathbf{I}]^T$  and  $\hat{\mathbf{d}} = [\mathbf{d}, \Theta_d \mathbf{g}^{\text{init}}]^T$ . After one iteration solving for  $\mathbf{g}^{\text{est}}$ , we obtain a first approxi-  
 472 mation to density that we note  $\mathbf{g}'$ . Substituting this density approximation into equation (25), we estimate  
 473 phase velocity using gradiometric methods where we write the discrete finite difference form of equation (25)  
 474 in terms of parameter  $\mathbf{g}'$  and estimate the phase velocity via linear regression similarly to (De Ridder and  
 475 Biondi, 2015):

$$\begin{aligned} \frac{1}{2\Delta x^2} & \left[ g'_{[0,-]} P_{[i,j-1]}^n + g'_{[-,0]} P_{[i-1,j]}^n - g'_{[\pm,\pm]} P_{[i,j]}^n \right. \\ & \left. + g'_{[0,+]} P_{[i,j+1]}^n + g'_{[+,0]} P_{[i+1,j]}^n \right] c_{\omega,[i,j]}^2 = \left[ \frac{P_{[i,j]}^{n+1} - 2P_{[i,j]}^n + P_{[i,j]}^{n-1}}{\Delta t^2} \right] \end{aligned} \quad (37)$$

<sup>476</sup> where  $\mathbf{g}'_{[-,0]}$  and  $\mathbf{g}'_{[0,-]}$  are written similarly to

$$\mathbf{g}'_{[+,0]} = \frac{\mathbf{g}'_{[i+1,j]}}{\mathbf{g}'_{[i,j]}} + 1 \quad (38)$$

$$\mathbf{g}'_{[0,+]} = \frac{\mathbf{g}'_{[i,j+1]}}{\mathbf{g}'_{[i,j]}} + 1 \quad (39)$$

<sup>477</sup> and

$$\mathbf{g}'_{[\pm,\pm]} = \mathbf{g}'_{[0,-]} + \mathbf{g}'_{[-,0]} + \mathbf{g}'_{[+,0]} + \mathbf{g}'_{[0,+]}$$

<sup>478</sup> In matrix form, equation (37) can be written

$$\mathbf{J}' \mathbf{m}' = \mathbf{d}' \quad (40)$$

<sup>479</sup> where  $\mathbf{m}' = [c_{\omega,[0,0]}^2, c_{\omega,[1,0]}^2, \dots, c_{\omega,[M,N]}^2]^T$  is the parameter vector of dimension  $[R \times 1]$ ,  $\mathbf{d}'$  is an observed data  
<sup>480</sup> vector of dimension  $[R \times n_t]$  that contains time derivatives of the recorded pressure field and coefficient matrix  
<sup>481</sup>  $\mathbf{J}$  of dimensions  $[R \times R \times n_t]$  contains knowledge about the pressure wavefield gradients and density gradients  
<sup>482</sup> from the full acoustic wave equation formulation. In the case of real data, where amplitude differences in the  
<sup>483</sup> wavefield due to site effects or difference in sensors can impact the data, it might be necessary to impose the  
<sup>484</sup> condition that medium parameters should not vary rapidly as a function of space (De Ridder and Biondi,  
<sup>485</sup> 2015). This can be achieved by adding a damping term, i.e., penalizing the second order spatial derivatives  
<sup>486</sup> in the form of a Tikhonov regularization. For the purpose of this paper, where we analyse synthetic data only  
<sup>487</sup> and the problem is well constrained, equation (37) is solved by linear regression with a mean squared cost  
<sup>488</sup> function, i.e., non-regularized least-squares WEI. Information about density obtained from equation (36)  
<sup>489</sup> and the updated phase velocity estimates obtained by solving equation (37), provide an updated estimate  
<sup>490</sup> of  $\mathbf{h}$  denoted  $\mathbf{h}'$ :

$$\mathbf{h}' = \frac{\mathbf{g}'}{\mathbf{m}'} \quad (41)$$

<sup>491</sup> and  $\mathbf{g}^{\text{init}}$  is updated by  $\mathbf{g}'$ . We proceed to perform several iterations of solving equations (36) and (37) until  
<sup>492</sup> we observe convergence towards a stable estimate of  $\mathbf{g}'$ . In the following we analyse this methodology for  
<sup>493</sup> acoustic media, then test its performance in elastic media.

494 **3.2 Volumetric arrays**

495 To estimate density with volumetric gradiometry in an elastic medium, a 2-step procedure is implemented.  
 496 First we discretise eq. (18) with finite differences on the volumetric array (Fig. 2b) and estimate body wave  
 497 velocities with linear inversion techniques based on the free surface methodology described in Curtis and  
 498 Robertsson (2002). We employ a standard non-regularized, least-squares minimization technique to estimate  
 499  $v_S'$  and  $v_P'$ . Second, we discretise left- and right-hand sides of eq. (23) with classical finite differences and  
 500 substitute in the estimated body wave velocities  $v_S'$  and  $v_P'$  obtained from WEI:

$$\underbrace{\left[ \partial_t^2 u_z + v_P'^2 \left[ -\frac{2}{\Delta z} [\partial_z u_z]_{fd} + \nabla_H^2 u_z \right] - 2v_S'^2 \nabla_H^2 u_z \right]_{[i,j,0]} }_{lhs} = \frac{1}{\rho_{[i,j,0]}} \underbrace{\left[ \frac{1}{\Delta z} \left( 2 - \frac{4v_S'^2}{v_P'^2} \right) P \right]_{[i,j,0]}}_{rhs} \quad (42)$$

501 where,

$$lhs_{[i,j,0]} = \frac{u_{z[i,j,0]}^{n+1} - 2u_{z[i,j,0]}^n + u_{z[i,j,0]}^{n-1}}{\Delta t^2} - \frac{2}{\Delta z} v_{P[i,j,0]}' \left[ \frac{u_{z[i,j,-1]} - u_{z[i,j,0]}}{\Delta z} \right] \\ + \left( v_{P[i,j,0]}'^2 - 2v_{S[i,j,0]}'^2 \right) \frac{u_{z[i,j-1,0]}^n + u_{z[i-1,j,0]}^n - 4u_{z[i,j,0]}^n + u_{z[i+1,j,0]}^n + u_{z[i,j+1,0]}^n}{\Delta x^2} \quad (43)$$

502

$$rhs_{[i,j,0]} = \frac{1}{\rho_{[i,j,0]}} \left[ \frac{1}{\Delta z} \left( 2 - \frac{4v_{S[i,j,0]}'^2}{v_{P[i,j,0]}'^2} \right) P_{[i,j,0]} \right] \quad (44)$$

503 which enables density to be estimated via linear regression at each receiver position  $[i,j,0]$  at the surface:

$$lhs_{[i,j,0]} = \frac{1}{\rho_{[i,j,0]}} rhs_{[i,j,0]} \quad (45)$$

504 **4 Synthetic Tests**

505 By using wavefield gradiometry we aim to image the shallow subsurface in as much detail as possible. With  
 506 the following synthetic study we wish to examine the role of density in enhancing or obscuring our resolution  
 507 of lateral heterogeneities.

508

509 We use the 3D wavefield modelling software Salvus (Afanasiev et al., 2019) to produce accurate synthetic  
 510 acoustic and elastic wavefield recordings in 3D heterogeneous media. The wavefield is recorded at the surface  
 511 over a  $40 \times 40$  receiver grid in the middle of the domain. As a rule of thumb in gradiometry, the wavefield  
 512 should be sampled at spatial points spaced a maximum of around 12% of the minimum wavelength apart,

in order to obtain an accuracy of 10% in first order spatial derivatives (Langston, 2007b). Analogous error calculations for second order derivatives suggest that for a same level of accuracy receivers must be spaced at a maximum of 24% of the minimum wavelength (Appendix A); in other words for the same receiver spacing, second order derivatives are less prone to large finite difference errors than first order derivatives. With a spacing of 2 m and a minimum medium velocity of 1550 m/s, this allows frequencies up to 180 Hz to be used with reasonable accuracy. All wavefields are recorded for a time interval of 3 s at a temporal sampling rate of 0.3 ms. A buried receiver is placed 1 m below every receiver on the surface array for volumetric gradiometry.

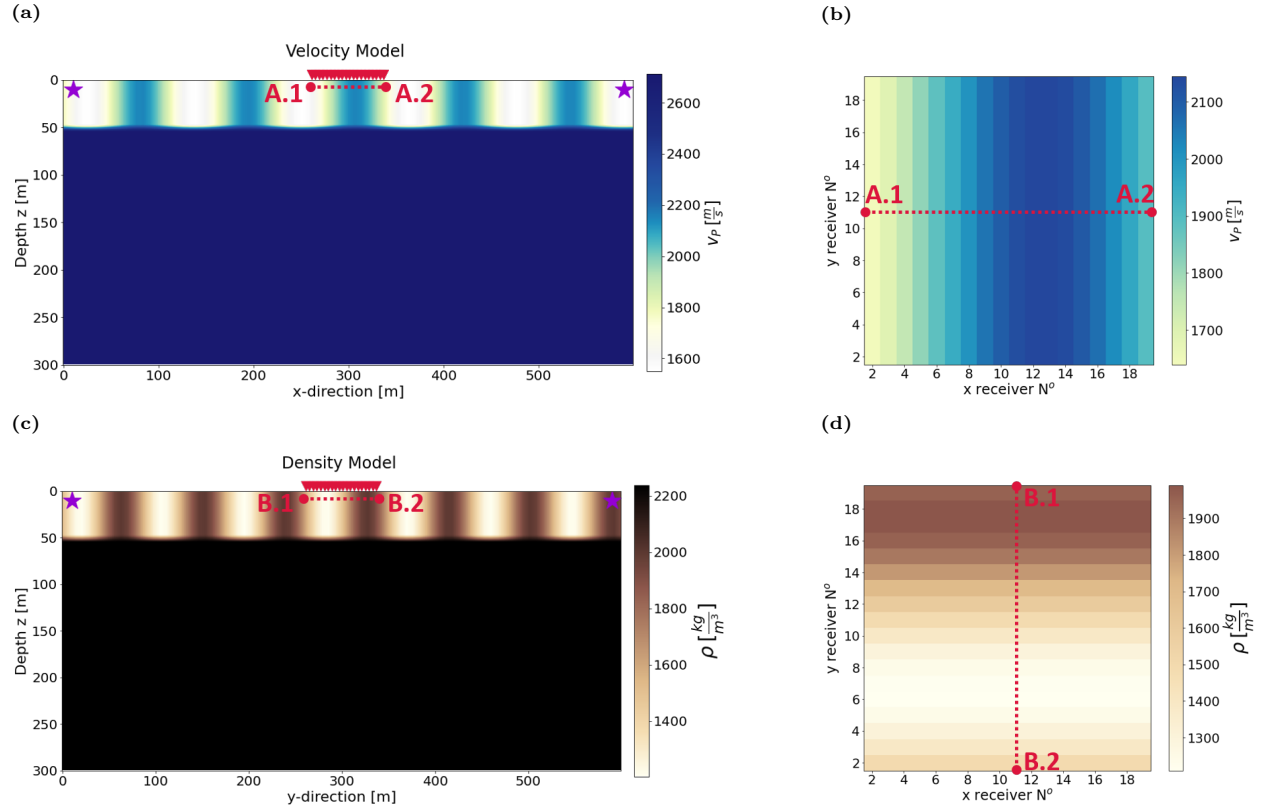


**Figure 3:** (a) Acoustic velocity model cross-section in xx-plane. Source locations relative to the receiver array are indicated by stars. Receiver groups marked by red triangles highlight the location of one line of 40 receivers at the surface and their corresponding buried receiver positioned at 1 m depth below. The total array spans an area of  $78 \times 78 \text{ m}^2$  spaced at 2 m intervals across the range [261, 339] m in both x and y directions. For gradiometry relying exclusively on the surface array, derivatives are calculated over a decimated receiver grid spaced at 4 m, whereas all surface receivers at 2 m intervals are used to perform volumetric gradiometry. All plan views showing model parameters are represented on the decimated grid at 4 m receiver spacing. (b) 2D xy-plan view map of the section of the true velocity model spanned by the internal receivers of the surface array. Depth boundary from layer 1 to layer 2 does not correspond to a step function change but a linear increase within the model cell that transitions between properties from the shallower layer to the deeper layer. (c) Density model depth cross-section in yz-plane. (d) 2D xy-plan view map of the section of the true density model spanned by the internal receivers of the surface array. For the pressure signals in Figure 4, a constant density model of  $1600 \text{ kg/m}^3$  is used instead for the top layer (Fig. B1). Elastic runs are performed with the same velocity and density structure and an additional shear-wave velocity field. Acoustic and elastic forward models have slightly different meshing criteria due to their respective minimum model velocities.

Relevant depth slices and plan view maps of the true acoustic P wave velocity and density model are shown in Figure 3. The velocity heterogeneity of the top layer follows a sine function in the x-direction at a wave-

length of approximately 113 m. The density structure has a wavelength of 88 m and is rotated by 90°  
respective to the velocity structure in order to clearly decouple influences of each parameter. The rotation  
of the orientation of density heterogeneities relative to those in velocity should reveal whether the estimated  
density structure contains artefacts caused by velocity heterogeneity and vice-versa. Layer 1 is 50 m thick  
and velocities span the range 1550 m/s to 2300 m/s, densities span 1200 kg/m<sup>3</sup> to 2000 kg/m<sup>3</sup>, while the  
deeper layer has a homogeneous velocity of 2700 m/s and density of 2240 kg/m<sup>3</sup>. The receiver array spans  
an area of 78 × 78 m<sup>2</sup> and captures at least half a wavelength of the heterogeneity in both velocity and  
density structures (Figs 3b and 3d). Elastic models are constructed analogously to Fig. 3 with an additional  
S wave velocity model related to P wave velocity by a Poisson ratio of 0.25.

532

To test the performance of WEI for simulated ambient noise, five isotropic sources are placed on a circle  
around the receiver array at a radius of 290 m from the midpoint. They fire Ricker wavelet signatures  
with different central frequencies ranging from 4.5 Hz to 16 Hz at random time intervals but with the same  
amplitude to examine whether WEI is robust against waves of overlapping frequency. The sources fire close  
to the surface at 10 m depth to ensure that the dominant wave energy travels along the surface, allowing  
the assumption that the pressure gradient in z-direction is small compared to horizontal directions. The  
increasing velocity with depth in the model ensures that the waves are dispersive as in the true Earth's  
subsurface.

541

In addition to the proof-of-concept synthetic model where density structure is orthogonal to the velocity  
structure, and which is discussed in the main body of the paper, we examine more realistic models that  
resemble natural borders between geological units more closely in Appendix D. Two true density model  
whose structure oscillate in parallel with the velocity structure of Figure 3(a) and (b) are analysed for the  
acoustic data case. In Figure D1(a) the density gradients follow the same sine curve as the velocity structure  
and are directly aligned with the velocity gradients (Figure D1b), whereas the density and velocity in Figure  
D2(a) and (b) both also vary in the x-direction but are spatially shifted with respect to each other.

549 **5 Density fingerprint**

550 **5.1 Free surface arrays**

551 **Sensitivity to relative density gradients in full acoustic wave equation**

552 The full acoustic wave equation (25) can be written in the form of the Helmholtz wave equation and a source  
553 term containing relative density gradients  $\nabla\varphi(\mathbf{x})/\varphi(\mathbf{x})$  acting on pressure gradients  $\nabla P(\mathbf{x}, t)$ :

$$\nabla^2 P(\mathbf{x}, t) - \frac{1}{c_\omega(\mathbf{x})^2} \partial_t^2 P(\mathbf{x}, t) = \frac{\nabla\varphi(\mathbf{x})}{\varphi(\mathbf{x})} \cdot \nabla P(\mathbf{x}, t) \quad (46)$$

554 Relative density gradients influence pressure gradients whenever a spatial density gradient  $\nabla\varphi(\mathbf{x})$ , that is, a  
555 laterally heterogeneous density structure, exists. Otherwise the term on the right-hand side of equation (46)  
556 becomes zero.

557

558 To illustrate the role that relative density gradients play in influencing wavefield gradients we conduct a  
559 synthetic experiment in which we compare Helmholtz and full acoustic spatial pressure gradients of a signal  
560 recorded at a single receiver station in the model shown in Figure 3 with variable density and velocity  
561 (Figs 4c and 4d) to one recorded in a model with the same velocity structure but where density is laterally  
562 homogeneous in the top layer at a fixed value of  $1600 \text{ kg/m}^3$  (Appendix B, Fig. B1) corresponding to the  
563 mean value of the top layer in the variable density model (Figs 4a and 4b). The spatial pressure gradients  
564 are expressed as

$$\nabla^2 P(\mathbf{x}, t) \quad (47)$$

565 for the Helmholtz equation 24 and

$$\varphi(\mathbf{x}) \nabla \cdot \left( \frac{1}{\varphi(\mathbf{x})} \nabla P(\mathbf{x}, t) \right) \quad (48)$$

566 for the full acoustic equation (25). For simplicity of notation, we drop the indication of space and time  
567 dependencies of density  $\varphi$  and pressure  $P$  hereafter. By comparing these spatial gradients in their discretized  
568 forms, we can establish a difference in discretization coefficients acting on pressure  $P$ , which subsequently  
569 influences the phase velocity estimates (Table 1). In the Helmholtz case, classical discretization coefficients  
570 for second order derivatives are used, whereas ratios of density from neighbouring receiver stations dominate

571 the discretization coefficients in the full acoustic case (equations 37 to 40). If the pressure field passes through  
 572 a homogeneous medium, the coefficients in the full acoustic case reduce to the Helmholtz coefficients since  
 573 ratios of adjacent density values are equal to 1: the phase velocity estimates are thus identical in this case  
 574 regardless of which equation is used for WEI. Whenever the densities between neighbouring receiver stations  
 575 vary, the full acoustic coefficients contain density ratios not equal to 1 and an effect on the phase velocity  
 576 estimate is expected depending on whether the Helmholtz or the full acoustic wave equation is used as a  
 577 basis for WEI.

578

**Table 1:** If divided by receiver spacing  $\Delta x^2$ , the presented values correspond to finite difference discretization coefficients on a regular grid (Fig. 2) for second order spatial pressure gradients in Helmholtz (24) and full acoustic (25) equations respectively. Helmholtz coefficients correspond to the classical central finite difference discretization values. Full acoustic coefficients are dependant on density ratios  $g'$  of neighbouring receivers.

	[j-1]	[i-1]	[i,j]	[i+1]	[j+1]
Helmholtz:	1	1	-4	1	1
Full Acoustic:	$\frac{1}{2} g'_{[0,-]}$	$\frac{1}{2} g'_{[-,0]}$	$\frac{1}{2} g'_{[\pm,\pm]}$	$\frac{1}{2} g'_{[+,0]}$	$\frac{1}{2} g'_{[0,+]}$

579 This behaviour of the spatial gradients becomes obvious in both acoustic (Figs 4a and 4c) and elastic (Figs  
 580 4b and 4d) media. In the homogeneous model case, Helmholtz and full acoustic spatial gradients are the  
 581 same, resulting in no difference between Helmholtz and full acoustic spatial gradients (Figs 4a and 4b). In  
 582 the model with variable density we observe a clear change in wave amplitude and a phase shift between  
 583 spatial gradients which is prominent between recording times 1 s and 1.7 s in the acoustic case. After 1.7 s  
 584 changes in the shape of the waveforms of Helmholtz and full acoustic gradients are observed in the acoustic  
 585 example (Figure 4c). Density gradients therefore create a clearly distinguishable fingerprint (Figs 4c and  
 586 4d), especially in acoustic media. The difference in Helmholtz and full acoustic spatial gradients is affected  
 587 less strongly in elastic media even though underlying density gradient values are the same in both acoustic  
 588 and elastic models. The fingerprint  $\Gamma$  is defined as the difference between normalised spatial gradients:

$$\Gamma = [\varphi \nabla \cdot \left( \frac{1}{\rho} \nabla P \right)] - [\nabla^2 P] = \frac{\nabla \varphi}{\rho} \cdot \nabla P \quad (49)$$

589 In the analysed synthetic model, density varies exclusively in the y-direction, where  $\partial_x \varphi = 0$  and  $\Gamma$  reduces  
 590 to the form:

$$\Gamma = \frac{1}{\rho} \partial_y \varphi \partial_y P \quad (50)$$

591 Neglecting information on density structure results in Helmholtz gradients that are not representative of the

propagation medium. This causes the phase velocity to be either over- or underestimated by WEI when using the Helmholtz equation in a variable density medium.

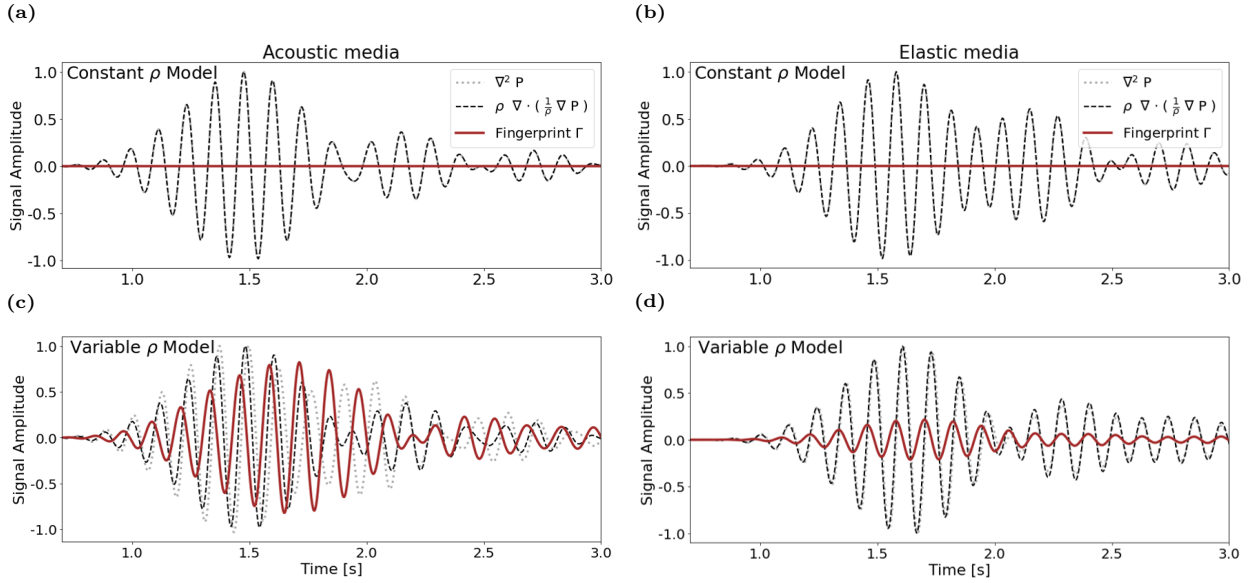


**Figure 4:** Effect of density gradients in 3D acoustic (a and c) and elastic media (b and d). Panel (a) and (b) show the discretized Helmholtz (dotted grey) and full acoustic (dashed black line) normalised spatial gradients at receiver [13,13] for a constant acoustic and elastic density model (Appendix B, Fig. B1) respectively. The difference between Helmholtz and full acoustic gradients (solid red line) shows that constant density has no influence on the measured wavefield. Panel (b) and (d) show the same information for a heterogeneous density model (Fig. 3c and 3d) in acoustic and elastic media respectively. The difference between Helmholtz and full acoustic gradients contains the signal generated by the density gradient in y-direction. The influence of the density gradient can clearly be distinguished (solid red line). In this example, the wavefield is filtered between 7 Hz to 9 Hz.

## 5.2 Volumetric arrays

### Sensitivity to density in free surface fully elastic wave equation

The linear equation derived from the vertical component of the Lax-Wendroff corrected full elastic wave equation puts constraints on density directly. Equation (45) shows that density linearly relates the temporal and spatial derivatives of displacement to the pressure term. In Fig. 5 it becomes clear that the left- and right-hand sides of eq. (45) are related by a scaling factor. By fitting a regression line with the slope of the inverse of true density in the heterogeneous forward model, a coefficient of determination  $R^2$  close to 1 is obtained suggesting that the scaling factor between left- and right-hand sides corresponds to the density of the medium. Fig. 5(b) shows that residuals are essentially zero between left-hand and right hand sides of eq. (45) if the true density is substituted. The density signal behaves analogously in homogeneous media.

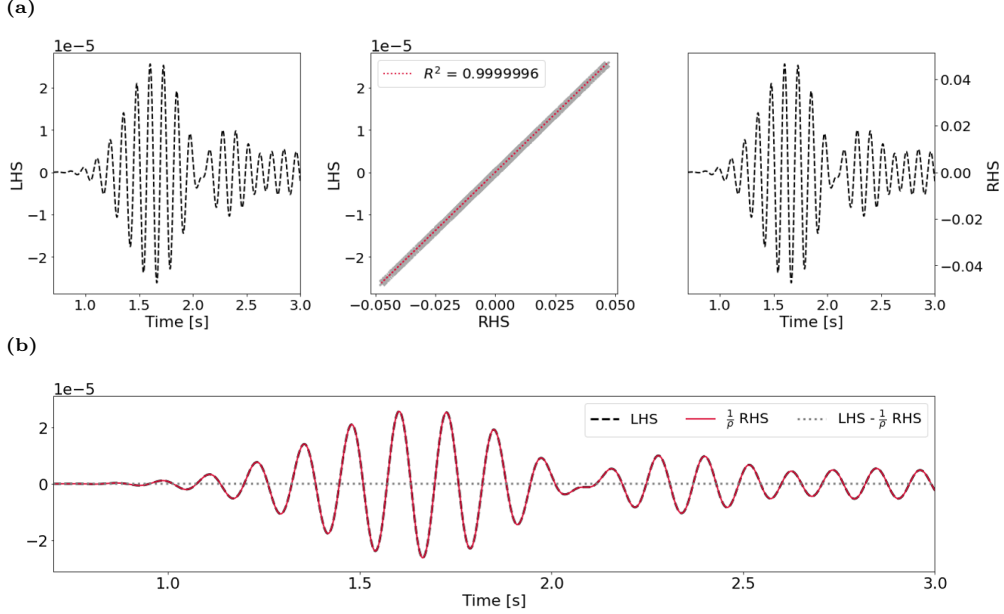


**Figure 5:** Role of density at the free surface of 3D elastic media (heterogeneous forward model (Fig. 3)) shown at the example receiver at location [13,13]. The wavefield is filtered around a central frequency of 8 Hz with a bandpass of 2 Hz. Panel (a) shows the waveform of the discretised left-hand side (left column) and right-hand side (right column) of eq. (45) when true velocity model parameters are used. The middle column in (a) shows a scatter plot of left- and right- hand data with a regression line of a slope corresponding to the inverse of true density at receiver [13,13].  $R^2$  is the coefficient of determination defining the goodness of fit of the regression line and the data. Panel (b) shows the residuals ( $LHS - \frac{1}{\rho} RHS$ ) between left- and right-hand side of equation (45) if the true model density is used.

## 6 Inversion Results

We now present results from the iterative inversion process for density and phase velocity using simulated ambient noise. In section 6.1.1 we investigate the performance of density estimation in acoustic media at a central frequency of 8 Hz where the wavefield data is filtered with a narrow bandpass in the range 7 Hz to 9 Hz. We then show how the obtained density information affects the accuracy of phase velocity estimates based on WEI of the full acoustic wave equation, and how random noise impacts the robustness of these estimates. We then investigate the quality of density inversion over a broader frequency range from 4 Hz to 14 Hz and the impact that full WEI has on estimates of phase velocity dispersion curves. In section (6.1.2) we discuss the estimated density results in elastic media for a wavefield filtered around 8 Hz obtained with the same iterative inversion workflow. Misfit functions are presented to illustrate trade-offs between density and phase velocity in both acoustic and elastic media (Section 6.1.3). We then show the density results in elastic media, obtained by gradiometric linear regression from the full elastic wave equation at the free surface (Section 6.2).

616

An outline of the structure of the result section summarising the analysed data types, array configurations and equation at the basis of the inversion methods, is given in Table 2.

**Table 2:** Overview of the used WEI approaches that structure the result section. For the inversion method based on free surface arrays (Fig. 2a) and volumetric arrays (Fig. 2b), used to produce the following results, the reader can refer to Section 3.1 and 3.2, respectively. For free surface arrays, the main underlying equation used to obtain density is the full acoustic wave equation (25). Density inversion with surface arrays, based on full acoustic WEI, is tested on both acoustic and elastic synthetic datasets. For volumetric arrays, density is obtained on the basis of a modified version of the full elastic wave equation (42) at the free surface in which both vertical particle velocity and pressure appear.

Array Type	Data medium	Equation for WEI
Free Surface (Section 6.1)	- Acoustic (Section 6.1.1) - Elastic (Section 6.1.2)	Full Acoustic (From Section 3.1, Eq. 25)
Volumetric (Section 6.2)	- Elastic (Section 6.2.1)	Modified Full Elastic Free Surface (From Section 3.2, Eq. 42)

## 619 6.1 Free surface arrays

### 620 6.1.1 Acoustic Data

#### 621 Density Estimation

622 Figure 6(a) shows the density inversion results as a mean over all cross sections in x (Fig. 6a, left) and y  
 623 direction (Fig. 6a, right). Corresponding lateral relative y- and x-gradients in density are depicted in Figure  
 624 6(b) in the left and right column respectively. Without damping, there is no constraint on the absolute value  
 625 of the density. Hence, the inversion process is quite sensitive to different initial damping parameters  $\Theta_d$ . As  
 626 a rule of thumb, setting the initial damping parameter at 10% of the mean amplitude of all recorded pressure  
 627 signals stabilized our inversions. The mean value over the true density model is fed to the inversion as the  
 628 initial homogeneous guess  $\rho_{\text{init}}$ .

629

630 We clearly see the effect of the damping term in the first iteration where the inverted density estimate is  
 631 skewed towards the initial guess. After the initial iteration we decrease the damping parameter by a factor  
 632 of 10 and keep it constant for a total of 100 iterations. Lowering the damping parameter gives less weight  
 633 to the prior information. Tests showed that the inversion process is only sensitive to the initial damping  
 634 parameter: decreasing the damping parameter further after the initial stabilization phase did not have an  
 635 effect on the final result, but it allowed the inversion to converge faster towards a minimum misfit solution.  
 636 After only 10 iterations of alternately updating velocity and density, the density estimates approximate the  
 637 true solution fairly well and remain stable over subsequent iteration steps until the end of the inversion  
 638 process is reached. The initial spiky character observed in x-direction might arise since we did not impose  
 639 any smoothness constraints on the inversion. The logarithm of the data misfit vector  $\delta_d$  of dimension [R×1]

$$\delta_d = \frac{\sum_{n=1}^{n_t} (\mathbf{J}'_n \mathbf{m}' - \mathbf{d}_n)^2}{n_t} \quad (51)$$

for the predicted model at each iteration is shown in Figure 6(c) and is used to determine whether the iteration delivers satisfactory results. At the initial iteration the logarithm of the full acoustic misfit of -7.0 is comparable to the Helmholtz misfit level at a value of -6.1. From there, the data misfit continually decreases with progressing iteration steps. In the first 10 iterations, the logarithmic misfit decreases rapidly from -7.0 to -13.2 at iteration 10. This steep drop correlates well with the improvement on the relative parameter error on the relative density gradient in y-direction. The relative error of parameter p at each location i,j is defined as the difference between the absolute values of true and estimated values  $|p|^{true}$  and  $|p|^{estimate}$  divided by the true values

$$|\text{Error}|_{i,j} = 100 \left| \frac{|p|_{i,j}^{true} - |p|_{i,j}^{estimate}}{|p|_{i,j}^{true}} \right| \quad (52)$$

where, in this instance, parameter p stands for the relative x- or y-density gradients  $\partial_x \rho / \rho$  and  $\partial_y \rho / \rho$  respectively but can stand for any other estimated quantity. In the case where the true value in equation (52) is equal to 0, the denominator is scaled by 1. After 12 iterations the logarithm of the misfit remains almost constant around a value of -13.5 and only improves marginally to -13.9 until the inversion is stopped at iteration 100. The density gradient result with minimum parameter error to the true model in x-direction is achieved at iteration step 21.

655

The slight increase in parameter error on density thereafter is likely to originate from the velocity updates dominating the misfit evolution. Velocity has a much stronger effect than the density since it appears squared in the full acoustic wave equation. We showed in Figure 4 that in a medium with homogeneous density the spatial gradient expressions from the Helmholtz and the full acoustic equation are identical and so phase velocity estimates remain unaffected by homogeneous densities across the array. Since density is constant in the x-direction, the true phase velocity is only dependent on density structure in the y-direction. Given the poor constraints on density in the x-direction the mean estimate on the density gradient in x-direction deviates, if only slightly ( $\pm 0.15\%$ ), from the true value of zero (Fig. 6b). This introduces artefacts in the phase velocity estimates which in turn influence density estimates negatively throughout the iterative process. Nevertheless, in our experiments the data misfit minimum does tend to indicate when parameter estimates are reasonably accurate. Cross-talk between density and velocity appears to be weak as density

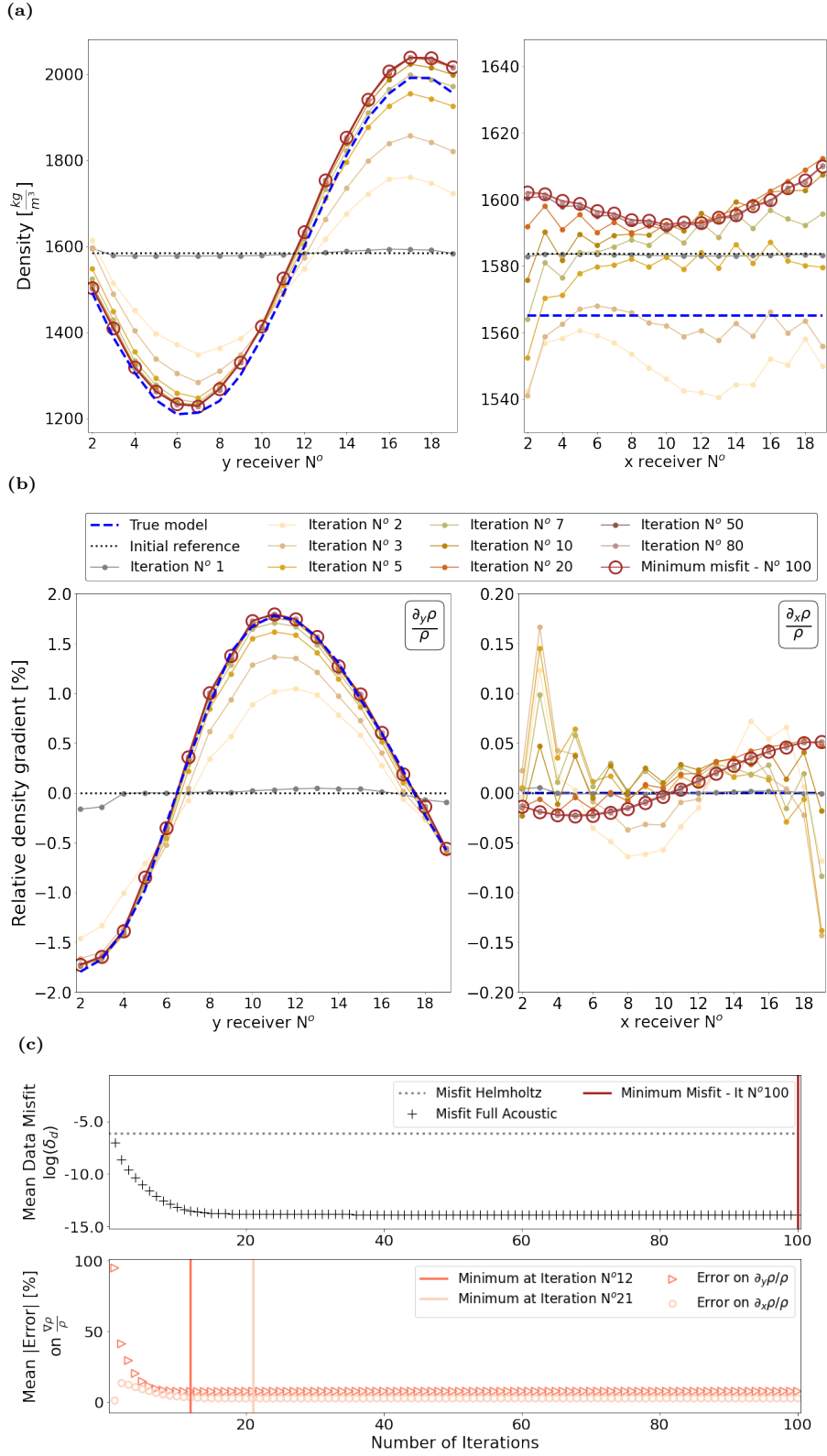


**Figure 6:** Inversion result for a wavefield filtered to include frequencies in the range of 7 Hz to 9 Hz. Only the results for the internal receivers 2 to 19 are displayed, as boundary stations need to be disregarded for finite difference estimates. (a) Mean value of inverted density results over all cross-sections in x-plane (left) and y-plane (right) showing the evolution of inverted density results at selected stages during 100 iterations. True model is depicted as dashed dark blue line and initial model as dotted black line. The minimum misfit result at iteration 100 is highlighted by red circles. (b) Relative density gradients  $\nabla\rho/\rho$  of (a) in y- and x-direction respectively. (c) Logarithm of the mean data misfit evolution over all internal receivers (upper row) and mean parameter error over all internal receivers on x- and y- relative density gradients (lower row) for the full acoustic wave equation (black crosses) over 100 iterations. Their respective minimum value positions are marked by vertical lines in red for minimum misfit at iteration 100, dark orange and light orange at iteration 12 and 21 for minimum parameter error on relative density y- and x-gradients. As a reference, the misfit achieved with linear regression based on the Helmholtz equation is shown by the dotted grey line. The minimum mean parameter error is evaluated only after the initial iteration.

667 structure of the true model could be reconstructed successfully with reasonable accuracy without major  
668 artefacts (Fig. 6).

669

670 Relative density gradient results for models with parallel gradients (e.g., density structure varying in the  
671 same direction as the velocity structure) are shown in Appendix D (Figure D1c and D2c) and could also be  
672 reconstructed without a significant increase in cross-talk compared to the models with density and velocity  
673 gradients orthogonal to each other. Misfits are higher by two to three orders of magnitude but still suggest  
674 a good agreement with the data (Figure D1d and D2d); also the evolution of the mean error on the relative  
675 density gradients is comparable to the tested model with orthogonal density and velocity structures.

676

677 As discussed in section 5, the inversion is predominantly sensitive to the relative changes in density  $\nabla\rho/\rho$   
678 where  $\nabla\rho$  corresponds to the gradient of density at a central point  $\rho = \rho_{i,j}$  over the finite difference stencil  
679 (cf. Fig. 2), and is less so to the absolute values  $\nabla\rho$  (Fig. 7). Figure 7 shows that the minimum misfit  
680 estimate of the local density gradient in the y-direction is typically within  $\pm 10\%$  of the true value for relative  
681 density changes larger than 0.5% over the width of the spatial finite difference stencil. The accuracy of  
682 estimates decreases for very weak relative changes below 0.5%. Estimates on absolute values may be biased  
683 depending on which initial density guess is fed to the first iteration of the inversion. Results in Figure 6(a)  
684 could successfully reconstruct absolute density values due to an appropriate choice of starting model  $\rho_{init}$ . If  
685 the initial guess of bulk density varies more strongly from the true values, the absolute estimates are under-  
686 or over-estimated according to the input starting model (Fig. 7a, left) because the inversion fits the relative  
687 changes in density ratios (Fig. 7a, right) as becomes obvious from equation (46). By reconstructing relative  
688 density changes, the results are unbiased by the choice of initial density model  $\rho_{init}$  (Fig. 7a, right). The  
689 results of relative density gradients for each local receiver position over the entire grid are shown in Figure  
690 8 as 2D plan view maps.

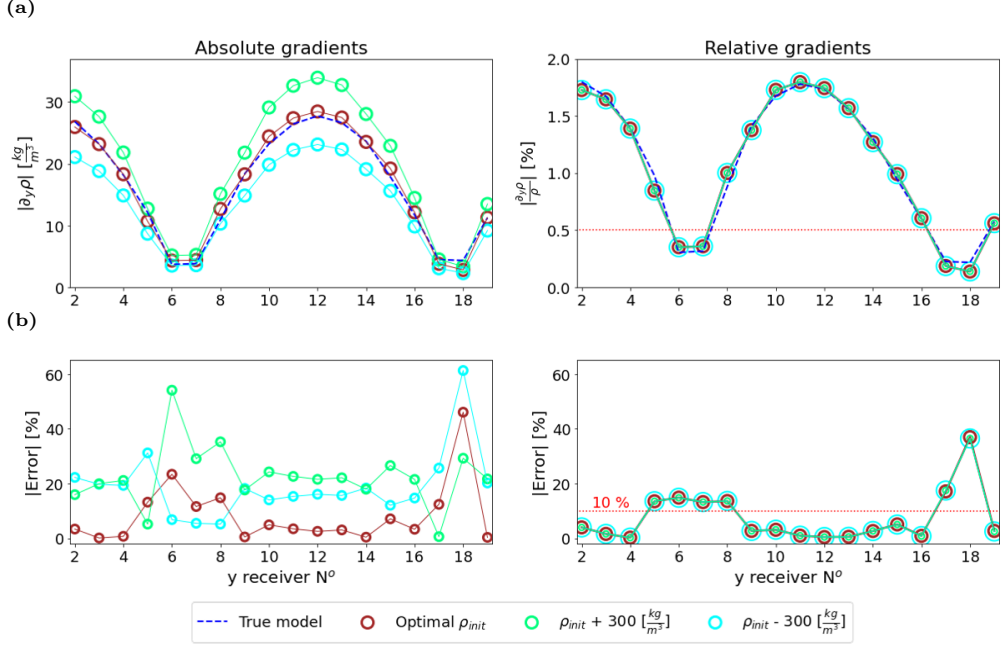


**Figure 7:** Impact of initial density guess  $\rho_{init}$  on inversion results of (a) absolute density y-gradients  $\partial_y \rho$  (left) and relative density y-gradients  $\partial_y \rho / \rho$  (right). Their respective errors (Eq. 52) are depicted in (b). Results from an optimal  $\rho_{init}$  starting model (red circles) correspond to the estimates in Figure 6(a) where  $\rho_{init}$  is the mean bulk density of the true model (dashed dark blue line). Results for a less well informed initial guess with higher mean bulk density (green circles) and lower mean bulk density (light blue circles) are shown for comparison.

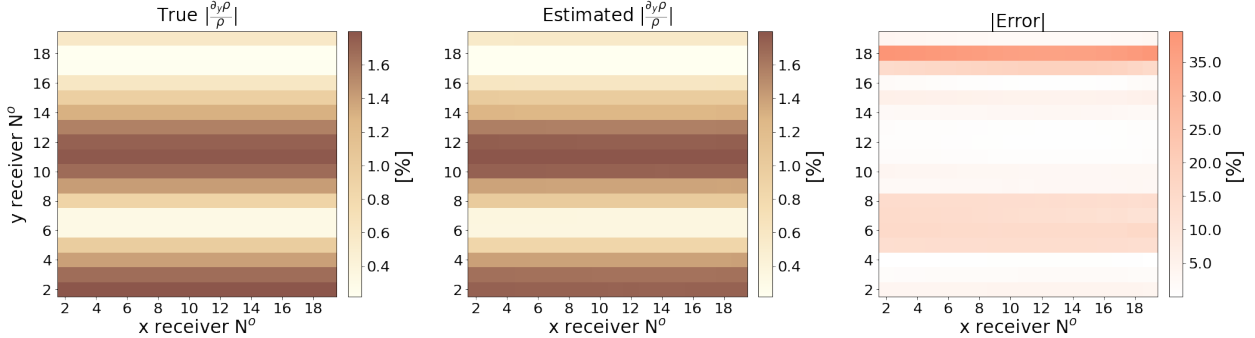


**Figure 8:** Plan view of (left) true model and (middle) inversion results for absolute values of relative density gradients in y-direction  $\partial_y \rho / \rho$  at iteration 100. The corresponding parameter error (Eq. 52) is shown in the right panel.

## 691 Effect of density gradient on phase velocity estimates

692 We now show the extent to which the estimated density structure influences the accuracy of the phase veloc-  
 693 ity maps. Figure 9(a) shows the phase velocity map estimated using the same data as above, but with the  
 694 Helmholtz wave equation, so without taking density into account in the formulation of wave propagation.  
 695 Figure 9(b) shows phase velocity estimates based on the full acoustic wave equation at iteration 100 where  
 696 the data misfit is minimal.

698 By visually comparing these maps to the true velocity structure (Fig. 3b) it is obvious that the Helmholtz  
699 approach fails to reproduce the relative structure of the subsurface velocity pattern. By contrast, the results  
700 obtained by WEI of the full acoustic wave equation yield an improved estimate of the velocity structure that  
701 is much closer to the true model in terms of relative structural features. This observation is reflected in the  
702 much lower misfit values obtained for the full acoustic model compared to the Helmholtz model (Fig. 9c). It  
703 is notable how the misfit evolution over the y-axis is dominated by the slope of the density heterogeneity in  
704 the true structure (red dashed line). The Helmholtz misfit values approach the full acoustic misfit values at  
705 a density gradient close to zero (see green highlight at y-receiver 6 in Fig. 9(c)), whereas, for steep changes  
706 in density at y-receiver 13 in the model, the Helmholtz equation performs relatively poorly.

707

708 Figure 10 illustrates the effect of density gradients on phase velocity estimates at two specific receiver  
709 stations in the array. Phase velocity squared is given by the slope of the linear relationship between spatial  
710 and temporal gradients (Equation (24) for Helmholtz and (25) for full acoustic equation). Figure 10(a)  
711 shows that the full acoustic spatial gradients reveal a clearer linear relationship than the Helmholtz model  
712 as indicated by a coefficient of determination  $R^2$  closer to 1. The difference in best fit slope estimates shows  
713 that phase velocity is considerably underestimated for the Helmholtz model at receiver [13,13] due to the fact  
714 that the relative density structure is neglected in the computation of the spatial gradients. This disparity in  
715 the accuracy of phase velocity estimates becomes evident also in the comparison of left-hand and right-hand  
716 side signals of the full acoustic and Helmholtz equation (Fig. 10b) and their respective residuals (Fig. 10c).  
717 They illustrate that the full acoustic expression matches the pure data vector well, whereas the Helmholtz  
718 expression exhibits larger residuals than the full acoustic case for both receiver stations. Incorporating  
719 density in the spatial gradient terms of WEI is thus shown to be important in order to estimate phase  
720 velocities accurately.

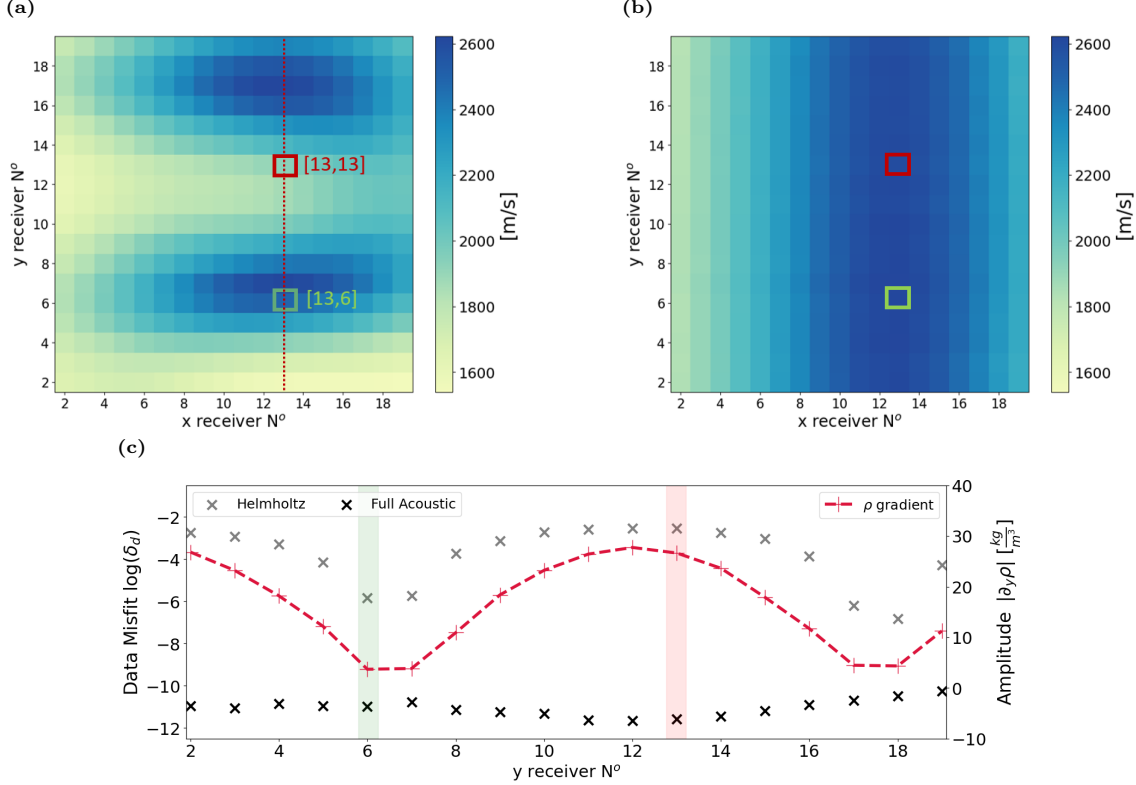
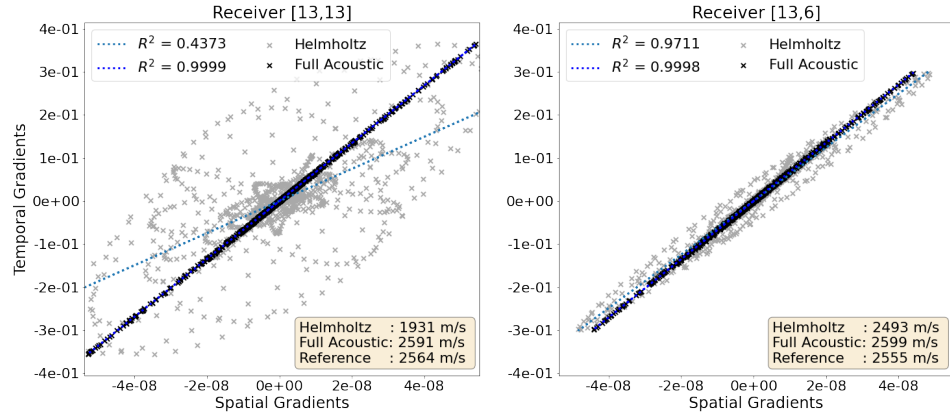


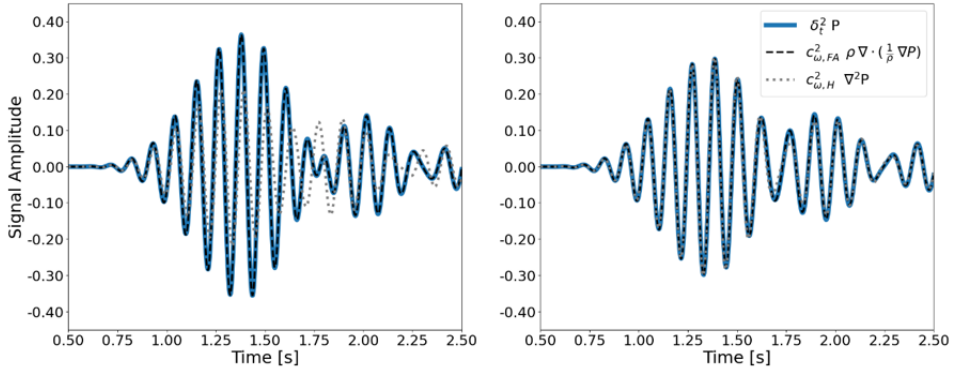
**Figure 9:** Phase velocity map estimated using (a) linear regression based on Helmholtz wave equation and (b) full acoustic wave equation inversion. Red and green squares mark receiver stations of interest [13,13] and [13,6]. (c) Data misfit post inversion averaged over all x-cross sections (red dotted line in (a) given at example of fixed receiver position  $x=13$ ) for both phase velocity maps (a) and (b). Black and grey crosses show the logarithm of misfit  $\delta_d$  in equation (51) for the Helmholtz equation (grey) and the full acoustic wave equation (black). The red dashed curve shows the absolute value of the y-gradient of the true density heterogeneity  $|\partial_y \rho|$ . Green and red highlighting at receiver station 6 and 13 represent the respective positions in the 2D plan view map.

If we compare the misfit residuals for receiver [13,13] (Fig. 10c, left) and [13,6] (Fig. 10c, right), we can see that the full acoustic residuals are of the same order of magnitude at both stations whereas the Helmholtz residuals are two orders of magnitude larger for receiver [13,13]. Receiver [13,13] is located in an area where density is highly variable between the surrounding stations ( $26 \text{ kg/m}^3$  from Fig. 9c) which explains why the Helmholtz wave equation is subject to much larger residuals than the full acoustic equation. Receiver [13,6] is in an area with only weak variations in density among neighbouring receivers ( $4 \text{ kg/m}^3$  from Fig. 9c), so the left-hand sides of both Helmholtz and full acoustic equations agree well with the observed data vector. The accuracy of velocity estimates thus depends on the true density gradient across surrounding receivers when using the Helmholtz equation for WEI.

(a)



(b)



(c)

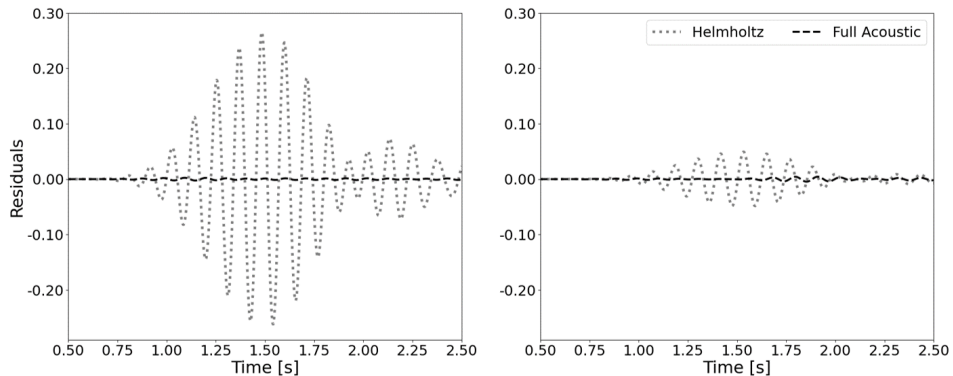


**Figure 10:** (a) Linear relationship between temporal gradients  $\delta_t^2 P$  and  $\rho \nabla \cdot (\frac{1}{\rho} \nabla P)$  from (48) for the full acoustic wave equation and  $\nabla^2 P$  from (47) for the Helmholtz wave equation at the two receiver locations shown in Figure 9(a). The coefficient of determination  $R^2$  denotes the goodness of fit of the data by the linear regression model, and phase velocity estimates using each equation are shown along with the reference velocity obtained for a homogeneous density forward model. (b) Discrete time series of the observed data vector ( $d = \delta_t^2 P$ , solid blue) and the left-hand sides of both Helmholtz ( $c_{\omega,H}^2 \nabla^2 P$ , black dotted) and full acoustic ( $c_{\omega,FA}^2 \rho \nabla \cdot (\frac{1}{\rho} \nabla P)$ , grey dashed) wave equations respectively, when using the estimated parameter values for phase velocity and density. (c) Respective residuals (difference between right-hand and left-hand side) of both Helmholtz and full acoustic wave equations.

730 **Changing data frequencies**

731 The effect of the density gradient on phase velocity is persistent over a wider frequency range than was  
 732 analysed above (Fig. 11a). In Figs 11(a) and 11(b), the dashed blue lines depict the true P-wave velocity  
 733 in y- and x-direction respectively for the shallow layer 1 and the deeper layer 2 of the synthetic model (Fig.  
 734 3). Due to wave dispersion, the estimated phase velocities should lie in between those two expected absolute  
 735 thresholds depending on the analysed frequency. The Helmholtz estimates for phase velocity (Fig. 11a) are  
 736 consistently underestimated for receivers where density gradients are high (see Fig. 12 as reference), due  
 737 to the use in WEI of discretization coefficients that neglect the influence of density (Table 1), whereas they  
 738 approximate full acoustic (Fig. 11b) phase velocity estimates at low density gradient values. However, the  
 739 influence of the density gradients on the Helmholtz phase velocity estimates seems to become smaller with  
 740 increasing frequency.

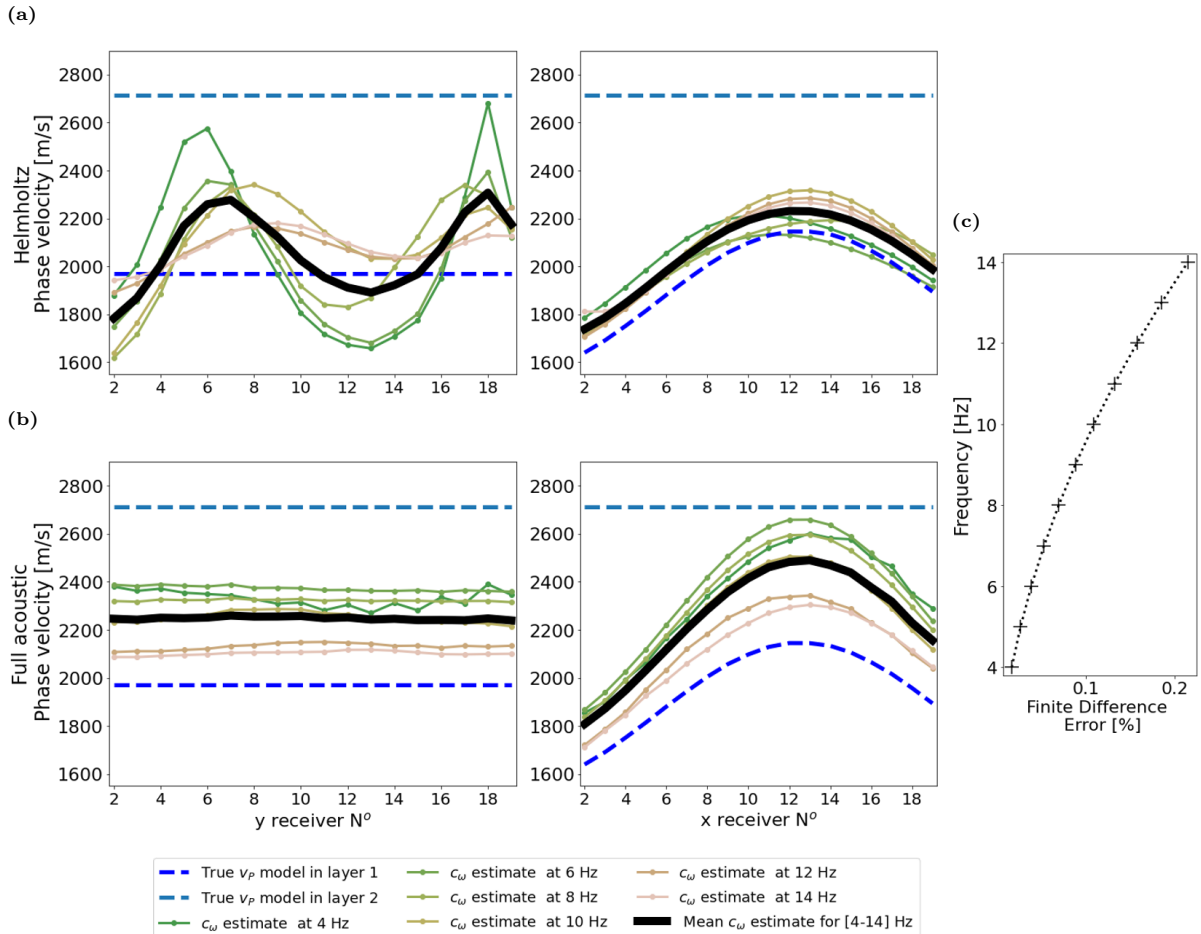


**Figure 11:** Results for the estimated phase velocities for 2 Hz wide bandpasses around central frequencies 4 Hz, 6 Hz, 8 Hz, 10 Hz, 12 Hz and 14 Hz from Helmholtz linear regression (a) and full acoustic WEI (b). For the estimation of full acoustic phase velocities, density information as shown in Figure 12 is used. The mean value over all the frequency results is shown for both full acoustic and Helmholtz velocities in a black solid line. (c) shows the error evolution over frequency for the 2<sup>nd</sup> order accurate approximation of the spatial gradients with a spacing of 4 m used in this example (see Appendix A).

741 Accuracy of density gradient estimates seems to decrease with increasing frequency (Figure 12): at a fre-  
 742 quency of 4 Hz, the true gradient model in layer 1 is well approximated, whereas the result at frequency  
 743 14 Hz shows a clear discrepancy between true and estimated density gradients. A trend between errors on  
 744 density gradients and strength of the density fingerprint (Fig. 12, right) becomes noticeable: parameter  
 745 errors on estimated density gradients via WEI increase with decreasing strength of the density signal. This  
 746 suggests that higher frequencies are less sensitive to density.

747

748 For the tested model, no frequency dependence of the relative density gradient estimate is observed. This  
 749 is likely due to the fact that the lower layer of the investigated model is homogeneous and consequently  
 750 does not have an associated density fingerprint. From Figure 7 we know that the bulk density estimate is  
 751 influenced by the damping parameter of the inversion process. Testing the frequency dependence on the  
 752 absolute density is possible if we hold the initial guess in the inversion process constant over the narrow  
 753 band-passed frequency bands. Figure C1 in Appendix C shows that there is no clear increase of the absolute  
 754 density estimate with decreasing frequency and thus the higher bulk density of the homogeneous lower layer  
 755 does not seem to influence the estimates.

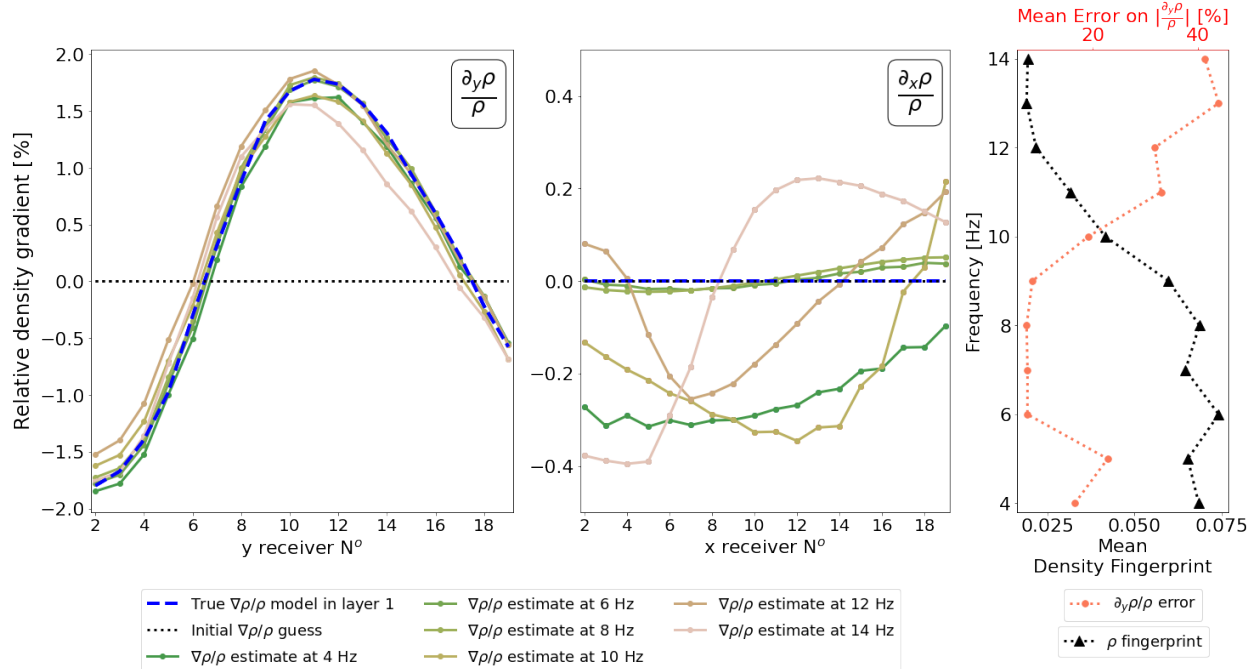


**Figure 12:** Results for density inversion at the lowest misfit iteration for 2 Hz wide bandpasses around central frequencies 4 Hz, 6 Hz, 8 Hz, 10 Hz, 12 Hz and 14 Hz. Estimated density is shown as a mean over all x (left panel) and y (middle panel) cross-sections respectively. The right panel shows the mean error (Eq. 52) on relative y-gradients of density averaged over the whole array per analysed frequency. The mean density fingerprint (Eq. 49) is calculated for each frequency as  $1/n_t \sum_{n=1}^{n_t} |\Gamma_n|$  and then averaged over the array.

756 Figure 13(d) shows how phase velocity perturbation increases with decreasing frequency and is roughly

757 correlated with the signal strength of density. Full acoustic WEI can account for these density induced  
 758 effects in phase velocity over a broad range of central filter frequencies, producing more accurate dispersion  
 759 curves (Figs 13a to 13c). The full acoustic estimates display higher coefficients of determination (Fig. 13b)  
 760 and lower misfits (Fig. 13c) than the Helmholtz results over all frequencies. As a reference we estimate a  
 761 dispersion curve for the velocity model in Figure 3 with a constant density of  $1600 \text{ kg/m}^3$  in layer 1 (Appendix  
 762 B, Fig. B1) and compare it to dispersion curves obtained with full acoustic and Helmholtz WEI (Fig. 13a)  
 763 for the variable density model (Fig. 3). The dispersion curve calculated on the basis of full acoustic WEI  
 764 is able to reproduce the general trend of the reference dispersion curve. We do not expect a perfect match  
 765 as the imposed density structure in the laterally heterogeneous case does influence the paths taken by wave  
 766 energy. The Helmholtz dispersion curve does not reproduce the key feature of a classical dispersion curve  
 767 where phase velocity increases with decreasing frequency. This shows that it is detrimental for depth model  
 768 reconstruction to assume a constant density over space in a medium with laterally heterogeneous density,  
 769 especially at lower frequencies.

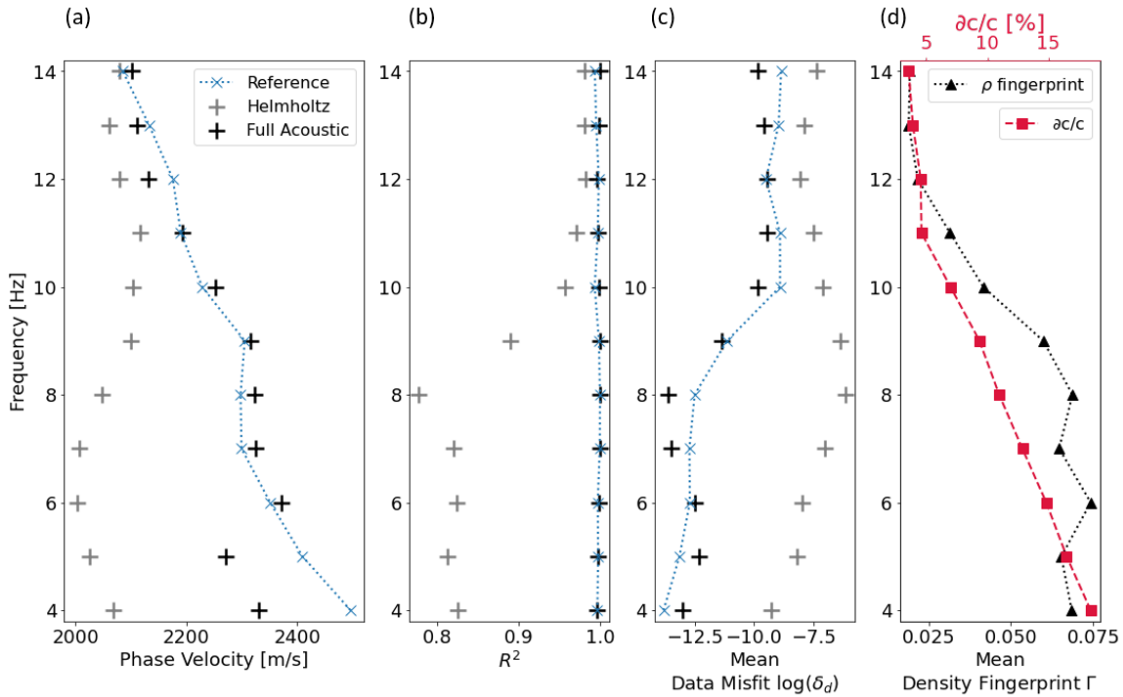


**Figure 13:** Mean phase velocity dispersion curve (a) over the whole array obtained via Full Acoustic WEI (black crosses) and Helmholtz WEI (grey crosses) respectively. Phase velocity results are obtained for a reference model (blue dotted line with cross marker) produced by the same setup as described in Figure 3 but with constant density in layer 1 (Appendix B, Fig. B1). Corresponding coefficients of determination (b) and misfits (c) are shown to evaluate the data fit. (d) The perturbation of phase velocity  $\frac{\partial c}{c}$  (red dashed line with square markers) is defined by the difference between phase velocity in the heterogeneous (grey crosses) and homogeneous baseline model (blue crosses) obtained via linear regression on the basis of the Helmholtz wave equation. The mean fingerprint  $\Gamma$  of the density signal is defined as in Fig. 12 and shown by black triangles.

770 **Random noise**

771 Given that in real use case scenarios WEI depends on field recordings, it is important to consider the robust-  
772 ness of density estimation to errors in the recorded signal. The density signal is relatively weak compared  
773 to that of phase velocity, hence it may be obscured by instrumentation noise in the field. We add random  
774 noise, expressed as a percentage of the mean trace amplitude over the whole grid, to the simulated observed  
775 signals in order to determine a threshold of noise beneath which the method still delivers meaningful results.  
776 For each receiver, the added noise follows an uncorrelated normal distribution with a spread of 0.1 to 5% of  
777 the mean trace amplitude.

778

779 Correlation factors for density decrease with increasing noise levels. At noise levels 0.1 to 1% of the mean  
780 trace amplitude, the pressure with added noise remains relatively similar to the true pressure (Fig. 14a). The  
781 density distributions are thus centred around the optimal correlation line where true and estimated density  
782 match perfectly (Fig. 14b). At a random noise level of 5% the density distribution does not approximate  
783 the optimal correlation line well which suggests that the relative density structure cannot be estimated  
784 accurately. The correlation of phase velocity is dominated by the quality of the density information and  
785 vice-versa: correlation coefficient values follow the same deteriorating trend when the noise level becomes  
786 higher (Fig. 14c). The estimates for both phase velocity and density remain stable up to a noise level of 1%,  
787 but even at a noise level of 5% the main structural trends are still recognised.

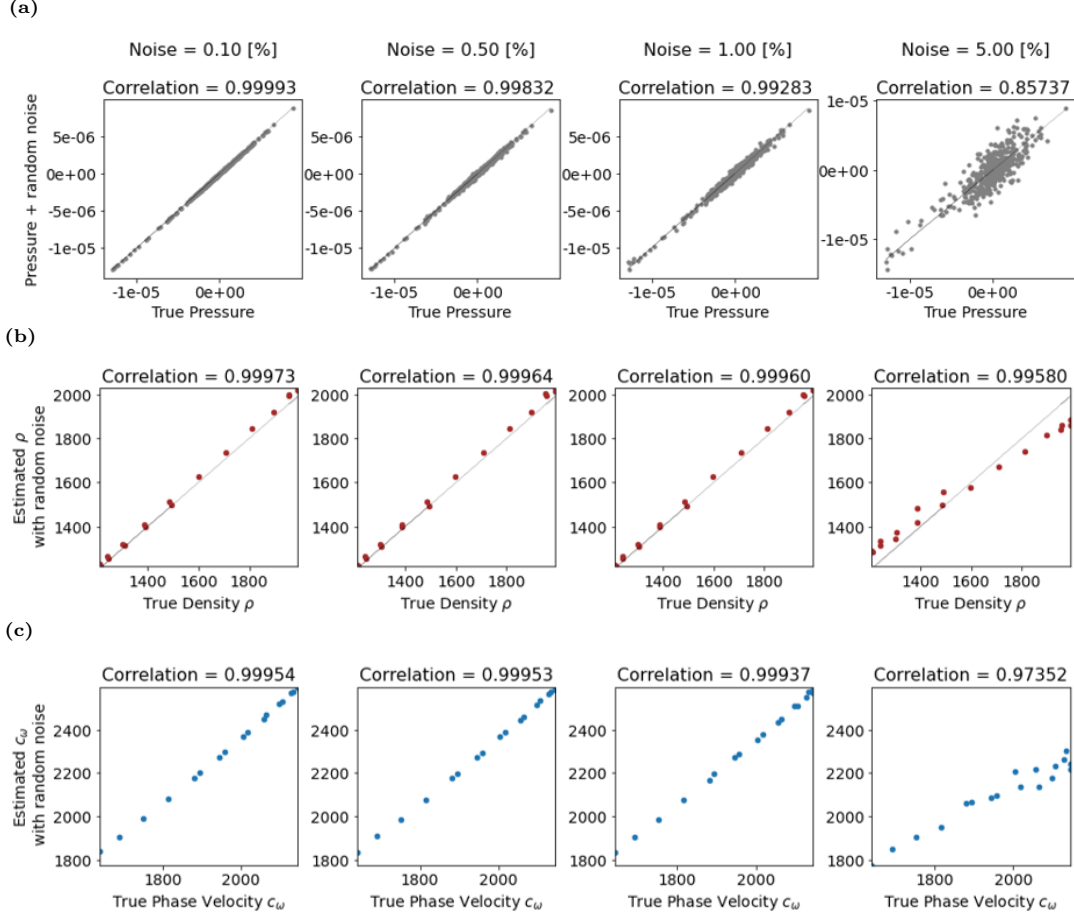


**Figure 14:** (a) Correlation plots between true pressure signal and pressure signal with added random simulated instrumental noise at 0.1 %, 0.5 %, 1 % and 5 % of the mean amplitude of the modelled pressure signal over the whole grid. Wavefield arrivals at  $t > 2$ s are used to visualise the effect of the added random noise on lower amplitude signals. Correlation plots of model material parameters at the various noise levels; between true and estimated (b) density and (c) phase velocity. True phase velocity is taken as  $0.9v_s$  of the surface layer, hence the frequency dependance is not taken into account as it is difficult to determine the expected phase velocity in a laterally heterogeneous medium.

788

### 789 6.1.2 Elastic Data

790 The iterative full acoustic inversion procedure is performed in an elastic medium for the calculated wavefield  
 791 potential  $\Phi$  (from eq. 7) for a central frequency of 8 Hz. The damping applied had to be 10 times stronger  
 792 than in the acoustic case, with the damping factor at the initial stabilizing iteration equal to the mean  
 793 amplitude of all recorded pressure signals. All subsequent iterations are carried out with 10% of the initial  
 794 damping. The obtained results for density (Fig. 15a) and relative density gradients (Fig. 15b) suggest that  
 795 the structural trends of the true model in the y-direction can be estimated approximately, but contain sub-  
 796 stantially more artefacts than in the acoustic case (Fig. 6). The sinusoidal trend of the lateral heterogeneity  
 797 in y-direction is recognisable but its shape is not approximated completely. These distortions are naturally

798 also mapped into estimates of spatial density variations. The poorly constrained results in the x-direction  
799 demonstrate relative density gradients deviating from zero, especially between receiver 3 to 6 which does not  
800 agree with the constant true model.

801

802 By examining the parameter error in x- and y-directions individually it becomes apparent that the parameter  
803 error in the x-direction monotonically increases with iterations, whereas the parameter error on the relative  
804 gradient in y-direction at first steadily decreases until iteration 60 after which it also follows an increasing  
805 trend. Consequently, artefacts are mapped into the density result during the inversion process. False  
806 structural density features are thus estimated by the inversion which suggests a strong cross-talk with other  
807 material parameters. A trade-off with velocity could cause the trend in velocity gradients in the x-direction,  
808 thereby distorting density. By mapping a false trend originating from the velocity error into the x-direction  
809 gradient, gradients in y-direction might compensate by over or under-estimating the density variation. The  
810 inversion being strongly influenced by the velocity response suggests that density has less weight in the elastic  
811 medium compared to the acoustic case. This becomes apparent in the misfit function map that explores the  
812 phase velocity and density space, displaying trade-offs between parameters in the acoustic and elastic case  
813 (Fig. 16).

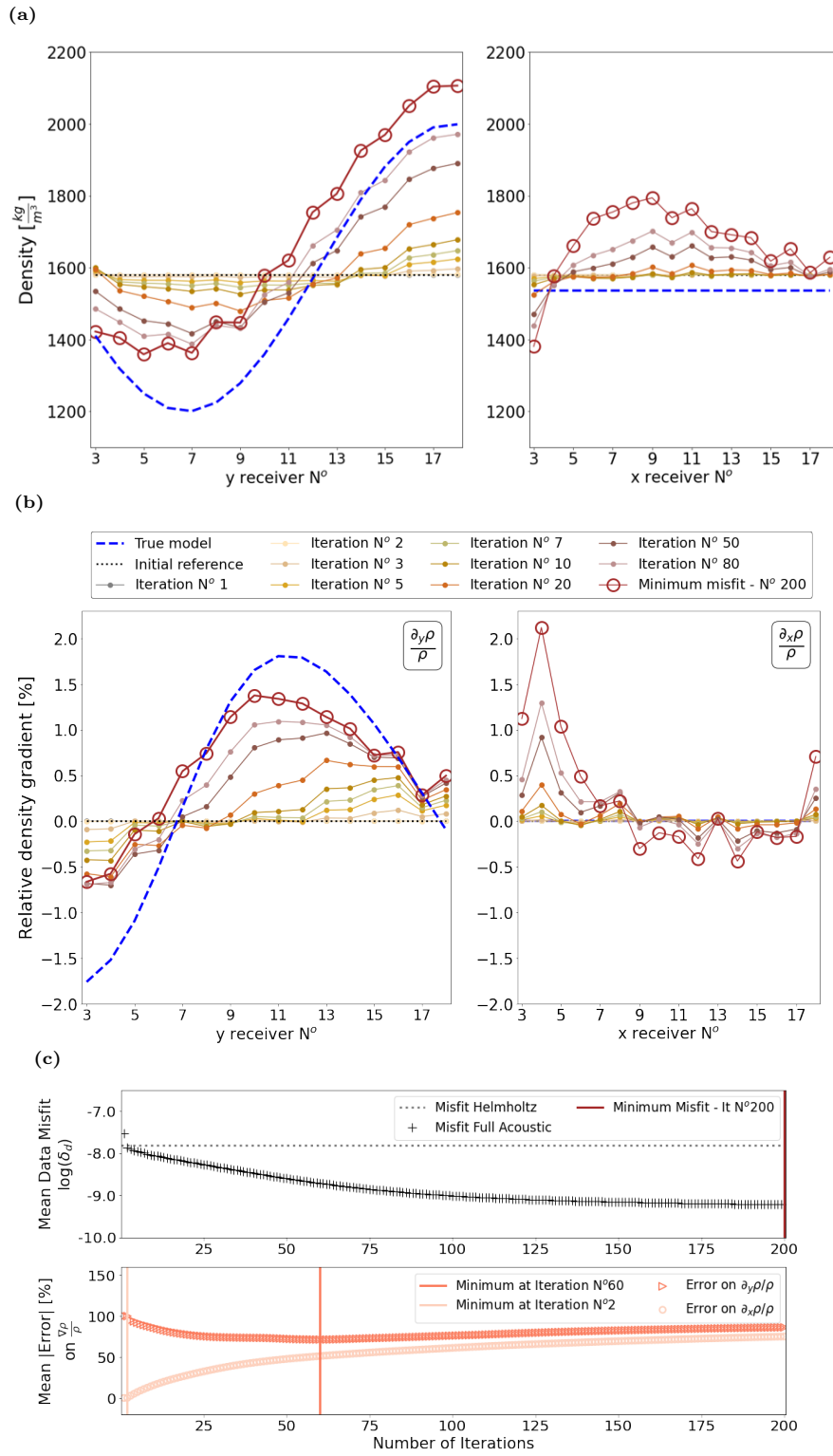


**Figure 15:** Inversion result for an elastic wavefield filtered to include a frequency range between 7 Hz to 9 Hz. Only the results for the internal receivers 3 to 18 are displayed, as boundary stations need to be disregarded for finite difference estimates and computing pressure entails an additional differentiation step in approximating the divergence of the displacement. Mean value of inverted (a) density and (b) relative density gradient results over all cross-sections in x-plane (left) and y-plane (right) showing the evolution of the inversion at selected stages during 200 iterations for a density model with sinusoidal heterogeneity as shown in Fig. 3. True model is depicted as dashed dark blue line and initial model as dotted black line. The minimum misfit result coincides with the last iteration 200 and is highlighted by red circles. (c) Logarithm of the mean data misfit over all internal receivers (upper row) for the full acoustic wave equation (black crosses) over 200 iterations. As a reference, the misfit achieved with linear regression based on the Helmholtz equation is shown by the dotted grey line. Mean parameter error on x- and y- relative gradients is shown in the lower row over all internal receivers. The respective minimum value positions are marked by vertical lines in red for minimum misfit at iteration 200, dark orange and light orange at iteration 60 and 2 for minimum parameter error on relative density gradients in y-direction and x-direction. The minimum mean parameter error is evaluated after the initial stabilizing iteration.

814 **6.1.3 Comparison between acoustic and elastic sensitivities**

815 To visualize the sensitivities of the inversion towards the investigated parameters, we perform a grid search  
816 where we analyse a grid of potential solutions for phase velocity and relative density gradients, and their  
817 misfit to the true model (Eq. 51) at a fixed central receiver location  $[x_0, y_0]$  (Fig. 16). The density at the  
818 central location is fixed at the true value, but both neighbouring cells in the y-direction are freely variable in  
819 order to investigate the misfit evolution for various relative density gradient values. The density at  $[y_0 + 1]$   
820 and  $[y_0 - 1]$  vary by  $\pm 25\%$  around the true density value at  $[x_0, y_0]$  and produce relative gradient values  
821 between  $\pm 6.25\%$ . The phase velocity at the central point is variable around the phase velocity at  $[x_0, y_0]$   
822 obtained by full acoustic WEI and spans a range of  $\pm 25\%$ .

823

824 We compare the misfit function for acoustic and elastic wavefield data at the central frequency of 8 Hz. At  
825 the example receiver [13,13], the global misfit minimum is about 3 orders of magnitudes lower in the acoustic  
826 case than in the elastic one. This suggests that more uncertainty is attached to the inversion process in the  
827 elastic medium given that wavefield traces have been normalised prior to the evaluation.

828

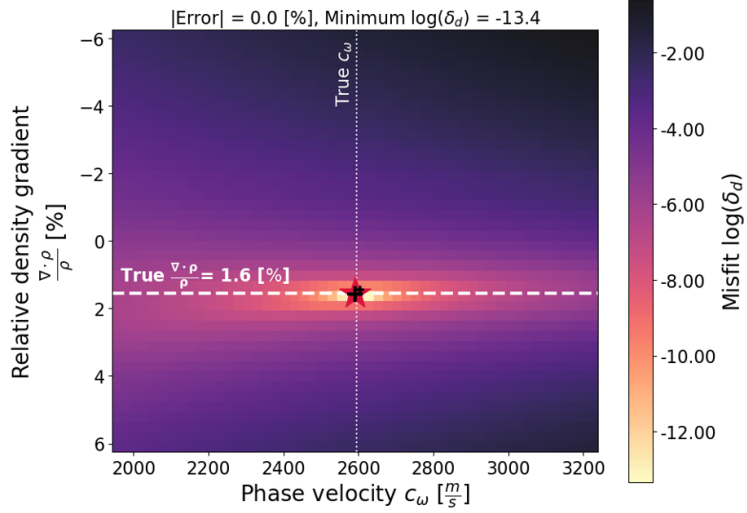
829 The misfit function distribution in the acoustic medium shows that density gradients are better constrained  
830 than phase velocities (Fig. 16a): for logarithm misfit values within two order of magnitude from the min-  
831 imum misfit (pink area,  $\log(\delta_d) < -11.4$ ), the phase velocity can vary up to 4% whereas the relative density  
832 gradient is better constrained with no fluctuation at all over the applied binning. The absolute minimum  
833 misfit coincides exactly with the true value of the relative density gradient ( $|Error| = 0\%$ ) and the minimum  
834 misfit phase velocity agrees well with the value of 2592 m/s obtained via full acoustic WEI using the true  
835 density structure. All iterations from the inversion process plot very closely to the global misfit due to the  
836 strong constraints on both parameters.

837

838 In elastic media, Figure 16(b) shows that a comparatively large number of relative density gradient and  
839 phase velocity values can explain the data on the basis of the full acoustic equation. For all solution pairs  
840 with misfit values within two orders of magnitude from the minimum misfit (pink to blue area on Fig. 16(b)),  
841  $\log(\delta_d) < -8.1$ , density gradients vary between 12.8% over the density gradient parameter space, whereas  
842 phase velocity fluctuates between 40.8% over the phase velocity parameter space. The comparatively higher  
843 uncertainty than in the acoustic case might be attributed to the weaker density signal strength (Fig. 4) and  
844 approximations in physics. An error of 12% between the true relative gradient and the global misfit value  
845 suggests that the elastic data can not be fully explained by an underlying full acoustic wave equation. This

implies that the inversion is prone to converge towards a slightly incorrect relative density gradient value.

(a) Acoustic



(b) Elastic

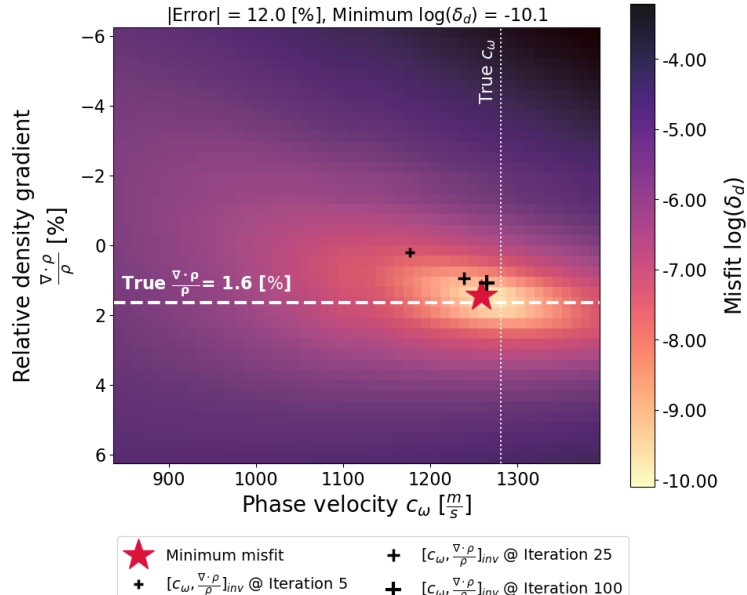


**Figure 16:** Misfit functions for (a) acoustic and (b) elastic media at receiver location [13,13] for a central frequency of 8 Hz. The misfit function are representative of the data used to produce Figs 6 and 15 respectively. The |Error| (eq. 52) shows the deviation of the relative density gradient value at the global minimum misfit in the grid search (yellow star) from the true value (white dashed line). Misfit is calculated as defined in eq. (51) and displayed for a single receiver. Crosses of increasing size show how total relative density gradient results of the iterative inversion process converges towards the global misfit of the grid search (small: iteration 5, medium: iteration 25, large: iteration 100). The true phase velocity  $c_\omega$  (thin white dotted line) denotes the phase velocity obtained from full acoustic WEI when the true density structure is known .

Iteration 5 of the inversion process gives an estimate on relative density gradient with a misfit value that is far away from the global misfit minimum (about two orders of magnitude) and provides a poor estimate on phase velocity and relative density gradient. Due to the comparatively poor constraints on both parameters,

850 subsequent iterations are subject to parameter cross-talk and artefacts are mapped into the solution, cor-  
851 rupting primarily the relative gradient in the x-direction. Nevertheless, the inversion manages to converge  
852 towards a value in the vicinity of the true relative density gradient. To test the gradiometric estimate on  
853 phase velocity at the investigated receiver location, we use the surf-96 code (Herrman, 2013) to calculate an  
854 expected value for mean Rayleigh wave velocity between 7 Hz to 9 Hz from the generated dispersion curve.  
855 The phase velocity value of 1260m/s corresponding to the lowest misfit marked by the yellow star in Figure  
856 16(b) is only 6% smaller than the expected value of 1340m/s generated by a 2 layer model matching the 1D  
857 depth structure at the receiver location in our true model.

858

859 In summary, both acoustic and elastic media show sensitivity to relative density gradients. However, rela-  
860 tive density gradients might not cause a large enough perturbation in the elastic wavefield to be sufficiently  
861 constrained in the inverse problem, whereas in acoustic media they are indeed essential to explain the data.

862

## 863 6.2 Volumetric arrays

### 864 6.2.1 Elastic Data

865 In a first step using a volumetric array, body wave velocities are estimated for a wavefield filtered between  
866 7 Hz to 9 Hz using a least-squares inversion from eq. (18). Those velocity results (Fig. 17a) are substituted  
867 into equations (43) to (44) along with the calculated pressure. Pressure at the free surface is given in eq.  
868 (11), but we find that using only the related acoustic expression  $P = K_a \nabla_H \cdot \mathbf{u}_H$  delivers more reasonable  
869 inversion results for density. Figure 17 shows the estimated density results obtained by linear regression of  
870 eq. (45). The accuracy of the density results depends on how well the velocities can be estimated. The mean  
871 value of the absolute parameter error over the receiver grid (Fig. 17b, right) measures 3.04 % illustrating  
872 that the estimated results are close to the true parameter values. Once body wave velocities and densities  
873 are estimated, we can proceed to calculate Lamé parameters via empirical relationships: results are shown  
874 for the first Lamé parameter in Fig. 17(c).

875

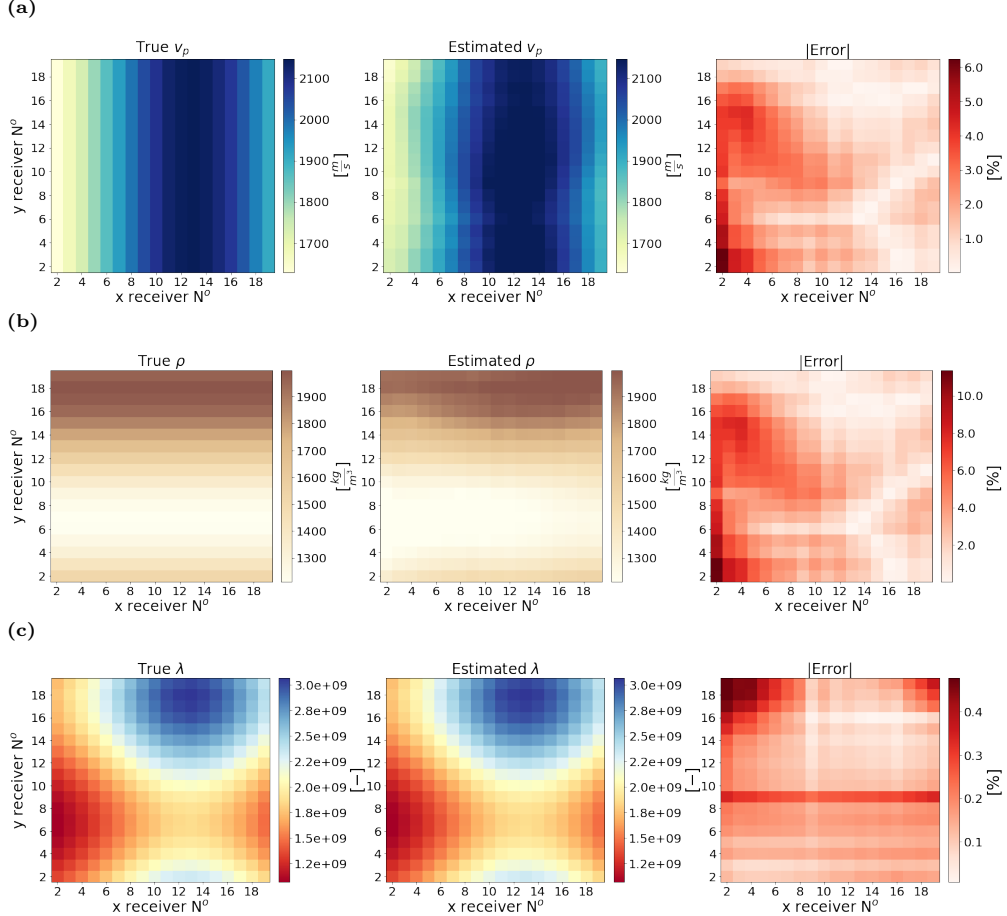


**Figure 17:** Plan view of (left column) true model and (middle column) gradiometric estimates of material parameters. The corresponding parameter error (Eq. 52) is shown in the right column. Rows (a), (b) and (c) correspond to results for P wave velocity, density and the first Lamé parameter  $\lambda$ . Velocities are estimated via WEI of eq. 18, densities by linear regression of eq. (45) and Lamé parameters are obtained from the latter estimated velocity and density results where  $\lambda = (v_p^2 - 2v_S^2)\rho$ .

## 876 7 Discussion

877 We have shown that in acoustic media, relative density gradients of 1.6% produce a substantial change  
 878 in the synthetic wavefield. This allows us to set up an inverse problem that successfully estimates den-  
 879 sity structure of the medium. The WEI approach has been demonstrated both at the example of models  
 880 where density and velocity structure are fully uncorrelated, as well as structurally more common models  
 881 that approximate geological interfaces. Density contrasts down to the amplitude of 0.5% can be imaged  
 882 with a parameter error smaller than 10% (Figure 7). First tests suggest that the inversion process is robust  
 883 for random noise up to 1% of the mean trace amplitude (Fig. 14) which encourages a future trial on real data.

884

885 In elastic media, other effects interfere with the density signal, making density estimation more difficult from

886 surface array data alone. Elastic results (Section 6.1.2) and sensitivity analysis (Section 6.1.3) show that  
887 there is sensitivity to relative density gradients in elastic media. However, the full acoustic approximation  
888 is too severe for elastic wave physics and density is too weakly constrained to be fully estimated using the  
889 proposed iterative inversion process. This makes it unlikely that density inversion based on gradiometric  
890 full-acoustic WEI will be feasible in an elastic Earth, or worse a visco-elastic Earth where the already  
891 small density signal might be overshadowed by the additional medium parameter of energy dissipation. The  
892 method might only be applicable in localized areas where the wavefield passes predominantly through gas  
893 or liquids.

894

895 To estimate density in elastic media it is therefore necessary to use volumetric array measurements and to  
896 adopt a more accurate representation of underlying wave physics as a basis for gradiometric WEI, such as  
897 the full elastic wave equation. However, it became clear from equation (3a) that if we only measure particle  
898 velocity or displacement and if the source term  $\mathbf{f}$  is omitted, density does not appear as an independent  
899 term outside of the expressions for body wave velocity. It is therefore impossible to estimate density inde-  
900 pendently of the Lamé parameters using a sourceless full elastic equation. However, if both displacement  
901 and pressure are measured in a dual sensor configuration, the full elastic wave equation at the free surface  
902 exhibits a direct, independent sensitivity to density in the form of a linear relationship between pressure and  
903 displacement terms (Section 6.2). If we are willing to deploy buried receivers then the results herein suggest  
904 that density can be estimated directly from recorded data, together with P and S velocities. Pressure sensors  
905 for solid earth applications have been presented as a prototype (Edme et al., 2018), but reliable pressure  
906 measurements are not readily available as of yet.

907

908 While our focus herein has been to make use of the ambient wavefield, an alternative exists if we consider  
909 the introduction of a local source within the receiver array. In that case, if the associated body force term  
910  $\mathbf{f}$  is clearly defined, density can be isolated within the wave equation and could in theory be estimated.  
911 We therefore propose a thought experiment in which we consider a weight drop within a 3D gradiometric  
912 receiver array (Fig. 1a) and perform volumetric gradiometry. If we assume that the weight drop acts as a  
913 vertical point load on the surface then the body force  $\mathbf{f}$  is generally defined as a distribution of force density  
914 as a function of position and time (Madariaga, 2007):

$$f(\mathbf{x}, t) = \mathbf{f}_0 s(t) \delta(\mathbf{x} - \mathbf{x}_0) \quad (53)$$

915 where  $\mathbf{f}_0$  is a unit vector in the direction of the point force  $\mathbf{f}_0 = [0, 0, 1]^T$ ,  $s(t)$  is a source time function

916 (the variation of the amplitude of the force as a function of time) applied in the vertical direction and  
 917  $\delta(\mathbf{x} - \mathbf{x}_0)$  is the Dirac distribution centered at the source location  $\mathbf{x}_0$ . Neitzel (1958) first analysed the seismic  
 918 characteristics of a weight-drop source in a field experiment: he measured the force applied to the ground  
 919 in an effort to characterise the source term and recorded the wavefield response. Several authors thereafter  
 920 proposed source term expressions to explain wavefield observations produced by a weight drop: based on  
 921 the work of Lamb (1904), Pekeris (1955) and Mooney (1974) derived analytical expressions of the wavefield  
 922 response at the free surface due to the application of an arbitrary excitation. The use of Heaviside step  
 923 function and Dirac Delta function could not reproduce wavefield quantities accurately, whereas a sinusoidal  
 924 source time function was shown to better approximate the generated wavefield (Abe et al., 1990). Defining  
 925 a generalised source term as accurately as possible is an essential task in predicting the Earth response to a  
 926 weight drop, and hence also in the proposed application to gradiometry. Colombero et al. (2015) found that  
 927 the source time function in the near-field of a weight drop can be represented by a modified Gabor wavelet  
 928 (based on Semblat and Pecker (2009)) expressed in terms of particle velocity:

$$s(t) = \begin{cases} C_b \beta t^\gamma \exp[-(\frac{2\pi}{T_s \alpha} t)^2] \cos(\frac{2\pi}{T_s} t) & \text{if } 0 \leq t \leq 1.2T_s \\ 0 & \text{otherwise} \end{cases} \quad (54)$$

929

930 where  $t$  is a generic time instant,  $T_s$  the period of the function,  $C_b$  the momentum of the dropped weight  
 931 and  $\alpha, \beta$  and  $\gamma$  are constants whose corresponding values are given in Colombero et al. (2015). By comparing  
 932 recorded particle velocity from drop load tests and synthetic data generated by propagating the proposed  
 933 source signal, they found that simulated and real impulse responses in the near-field of the source match well.

934

935 We therefore propose that in the case where we allow ourselves the luxury of a local source, the modified  
 936 Gabor source time wavelet (eq. 54) could in principle be incorporated in the volumetric gradiometry workflow  
 937 in order to estimate density on the basis of the full elastic wave equation at the free surface. Alternatively, one  
 938 could use a piezoelectric sensor as a controlled source using a preset electrical current signal (e.g., a Ricker  
 939 wavelet) to drive the resulting vibrations at the source point in the form of a known source time function. In  
 940 a first step we consider equation (3a) without body forces. We can then estimate P-wave velocity  $v_{P,e}$  and S-  
 941 wave velocity  $v_{S,e}$  at the free surface for any incoming wavefield using volumetric gradiometric measurements  
 942 and the Lax-Wendroff correction (Lax and Wendroff, 1964) as proposed by Curtis and Robertsson (2002).  
 943 Then by applying body forces in the form of a weight drop where  $s(t)$  is clearly defined (eq. 54), equation

944 (18) that describes the vertical component of a wavefield  $\vartheta = [\vartheta_x, \vartheta_y, \vartheta_z]$  at the free surface takes the form:

$$[\partial_t^2 \vartheta_z - v_{P,e}^2 A_z(t) + v_{S,e}^2 B_z(t)] \rho = f_z \quad (55)$$

945 with  $A_z(t)$  and  $B_z(t)$  given in equations (19) to (20). The entire left-hand side of equation (55) is then  
946 known apart from density, and takes the form of a linear inverse problem which might be solved for density.

947

948 Theoretically the response at the buried receiver could be inferred analytically by Green's function retrieval,  
949 if the effective volume encompassed by the gradiometric 3D receiver array is considered a uniform half-space  
950 in accordance with Lamb's problem. Johnson (1974) and Chen and Cao (2020) provide an expression of the  
951 Green's function at a buried receiver for a surface source over a homogeneous half-space. By extending this  
952 work to a Gabor wavelet source time function, the wavefield response at a buried receiver could be written  
953 analytically, reducing the acquisition requirements to a surface array.

## 954 8 Conclusion

955 We investigated whether surface wavefield gradiometry can be used to gain insights into material density  
956 via WEI of the full acoustic wave equation in both 3D acoustic as well as 3D elastic media using ambient  
957 noise data. We propose and test an iterative inversion scheme for both density and phase velocity based on  
958 gradiometric WEI and simulated ambient noise. No inherent scaling between velocity and density is imposed,  
959 making it suitable to detect density changes caused by temperature or chemically induced mechanisms. Syn-  
960 thetic results for 3D acoustic media suggest that it is possible to estimate relative density structure with  
961 WEI by using a full acoustic formulation for wave propagation along the surface. We show that using a  
962 constant density assumption for the medium can be detrimental to subsurface velocity images, whereas the  
963 full acoustic formulation of gradiometry improves our knowledge of all material properties. It allows us  
964 to estimate density as an additional material parameter as well as to improve phase velocity estimates by  
965 incorporating approximations of the density structure.

966

967 By expanding this methodology to the elastic case, we tested the feasibility of estimating density in the solid  
968 Earth with gradiometric WEI on the basis of a full acoustic approximation. The dilatational component of  
969 Rayleigh waves at the free surface was shown to be imprinted by effects from relative density changes in the  
970 medium. It proved however to be more difficult to obtain reliable estimates on relative density changes in  
971 elastic media than in acoustic media due to a stronger trade-off between density and phase velocity caused

972 by the difference in the measured wave type sensitivities to material parameters in both analysed media.  
973 However, using a 3D array and the full elastic wave equation at the free surface it is possible to obtain  
974 reliable absolute density estimates in elastic media. We suggest that another reasonable way to obtain  
975 density estimates in elastic media would be to fire a local source and include the corresponding source term  
976 within an inversion of the full elastic wave equation.

## 977 Acknowledgements

978 The present project was supported by the National Research Fund (FNR) of Luxembourg and by a Doctoral  
979 Training Partnership grant (NE/S007407/1) from the UK Natural Environment Research Council (NERC).  
980 The authors thank David Sollberger and one anonymous reviewer for their thoughtful comments that helped  
981 to improve the manuscript, as well as, Fern Storey and Andrew Valentine for editorial handling.

## 982 Data Availability

983 All code used in this study is publicly available at [https://github.com/mafab1994/density\\_WEI](https://github.com/mafab1994/density_WEI). The syn-  
984 thetic data was produced with the Salvus software package from Mondaic AG and is made available on the  
985 Zenodo repository <https://doi.org/10.5281/zenodo.10474217>.

## 986 References

- 987 Abe, S., Kobayashi, Y., & Ikawa, T. (1990). Seismic charac-1014  
988 teristics of the weight-dropping source. *Journal of Physics*1015  
989 *of the Earth*, 38(3), 189–212. 1016  
990 Afanasiev, M., Boehm, C., van Driel, M., Krischer, L., Ri-1017  
991 etmann, M., May, D. A., Knepley, M. G., & Fichtner, A. 1018  
992 (2019). Modular and flexible spectral-element waveform 1019  
993 modelling in two and three dimensions. *Geophysical Jour-1020  
994 nal International*, 216(3), 1675–1692. 1021  
995 Aki, K., & Richards, P. G. (2002). *Quantitative seismology*. 1022  
996 Amundsen, L., Røsten, T., Robertsson, J. O., & Kragh, E. 1023  
997 (2005). Rough-sea deghosting of streamer seismic data us-1024  
998 ing pressure gradient approximations. *Geophysics*, 70(1), 1025  
999 V1–V9. 1026  
1000 Anderson, S. P., von Blanckenburg, F., & White, A. F. (2007). 1027  
1001 Physical and chemical controls on the critical zone. *Ele-1028  
1002 ments*, 3(5), 315–319. 1029  
1003 Befus, K., Sheehan, A., Leopold, M., Anderson, S., & Ander-1030  
1004 son, R. (2011). Seismic constraints on critical zone archi-1031  
1005 tecture, boulder creek watershed. *Vadose Zone Journal*, 1032  
1006 10(3), 915–927. 1033  
1007 Bergmann, P. G. (1946). The wave equation in a medium 1034  
1008 with a variable index of refraction. *The Journal of the 1035  
1009 Acoustical Society of America*, 17(4), 329–333. 1036  
1010 Blanch, J., & Robertsson, J. O. (1997). A modified lax-1037  
1011 wendroff correction for wave propagation in media de-1038  
1012 scribed by zener elements. *Geophysical Journal Interna-1039  
1013 tional*, 131(2), 381–386. 1040  
Blom, N., Boehm, C., & Fichtner, A. (2017). Synthetic inves-1041  
1042 tions for density using seismic and gravity data. *Geophys-1043  
1044 ical Journal International*, 209(2), 1204–1220.  
Blom, N., Gokhberg, A., & Fichtner, A. (2020). Seismic wave-1045  
1046 form tomography of the central and eastern mediterranean  
upper mantle. *Solid Earth*, 11(2), 669–690.  
Boddice, D., Metje, N., & Tuckwell, G. (2019). Quantifying  
the effects of near surface density variation on quantum  
technology gravity and gravity gradient instruments. *Jour-1047  
1048 nal of Applied Geophysics*, 164, 160–178.  
Boddice, D., Metje, N., & Tuckwell, G. (2022). Microgravity  
1049 surveying before, during and after distant large earth-1050  
1051 quakes. *Journal of Applied Geophysics*, 197, 104542.  
Brimhall, G. H., Chadwick, O. A., Lewis, C. J., Compston,  
W., Williams, I. S., Danti, K. J., Dietrich, W. E., Power,  
M. E., Hendricks, D., & Bratt, J. (1992). Deformational  
mass transport and invasive processes in soil evolution.  
*Science*, 255(5045), 695–702.  
Cance, P., & Capdeville, Y. (2015). Validity of the acoustic  
approximation for elastic waves in heterogeneous media-ac-1052  
1053oustic approximation of elastic waves. *Geophysics*, 80(4),  
T161–T173.  
Cao, R., Earp, S., de Ridder, S. A., Curtis, A., & Galetti,  
E. (2020). Near-real-time near-surface 3d seismic velocity  
and uncertainty models by wavefield gradiometry and neu-1054  
1055 ral network inversion of ambient seismic noise. *Geophysics*,  
85(1), KS13–KS27.

- 1041 Chen, J.-B., & Cao, J. (2020). Green's function for three-dimensional elastic wave equation with a moving point source on the free surface with applications. *Geophysical Prospecting*, 68(4), 1281–1290.
- 1042 Choi, Y., Min, D.-J., & Shin, C. (2008). Frequency-domain elastic full waveform inversion using the new pseudo-hessian matrix: Experience of elastic marmousi-2 synthetic data. *Bulletin of the Seismological Society of America*, 98(5), 2402–2415.
- 1043 Colombero, R., Kontoe, S., Foti, S., & Potts, D. (2015). Numerical modelling of drop load tests. *Soil Dynamics and Earthquake Engineering*, 77, 279–289.
- 1044 Curtis, A., Gerstoft, P., Sato, H., Snieder, R., & Wapenaar, K. (2006). Seismic interferometry—turning noise into signal. *The Leading Edge*, 25(9), 1082–1092.
- 1045 Curtis, A., & Robertson, J. O. (2002). Volumetric wavefield recording and wave equation inversion for near-surface material properties. *Geophysics*, 67(5), 1602–1611.
- 1046 De Ridder, S., & Biondi, B. (2015). Near-surface scholte wave velocities at ekofisk from short noise recordings by seismic noise gradiometry. *Geophysical Research Letters*, 42(17), 7031–7038.
- 1047 De Ridder, S., & Curtis, A. (2017). Seismic gradiometry using ambient seismic noise in an anisotropic earth. *Geophysical Journal International*, 209(2), 1168–1179.
- 1048 Dexter, A. (2004). Soil physical quality: Part i. theory, effects of soil texture, density, and organic matter, and effects on root growth. *Geoderma*, 120(3-4), 201–214.
- 1049 Edme, P., Muyzert, E., Goujon, N., El Allouche, N., & Kragh, E. (2018). Seismic wavefield divergence at the free surface. *First Break*, 36(12), 75–82.
- 1050 Edme, P., & Yuan, S. (2016). Local dispersion curve estimation from seismic ambient noise using spatial gradients. *Interpretation*, 4(3), SJ17–SJ27.
- 1051 Fanchi, J. R. (2010). 7 - well logging. In J. R. Fanchi (Ed.), *Integrated reservoir asset management* (pp. 109–124). Gulf Professional Publishing. <https://doi.org/https://doi.org/10.1016/B978-0-12-382088-4.00007-4>
- 1052 Fichtner, A. (2010). *Full seismic waveform modelling and inversion*. Springer Science & Business Media.
- 1053 Flinchum, B. A., Holbrook, W. S., & Carr, B. J. (2022). What do p-wave velocities tell us about the critical zone? *Froniers in Water*, 3, 772185.
- 1054 Flinchum, B. A., Holbrook, W. S., Grana, D., Parsekian, A. D., Carr, B. J., Hayes, J. L., & Jiao, J. (2018). Estimating the water holding capacity of the critical zone using near-surface geophysics. *Hydrological Processes*, 32(22), 3308–3326.
- 1055 Foti, S., Hollender, F., Garofalo, F., Albarello, D., Asten, M., Bard, P.-Y., Comina, C., Cornou, C., Cox, B., Di Giulio, G., et al. (2018). Guidelines for the good practice of surface wave analysis: A product of the interpacific project. *Bulletin of Earthquake Engineering*, 16, 2367–2420.
- 1056 Friederich, W., Hunzinger, S., & Wielandt, E. (2000). A note on the interpretation of seismic surface waves over three-dimensional structures. *Geophysical Journal International*, 143(2), 335–339. <https://doi.org/10.1046/j.1365-246X.2000.01241.x>
- 1057 Gardner, G., Gardner, L., & Gregory, A. (1974). Formation velocity and density—the diagnostic basics for stratigraphic traps. *Geophysics*, 39(6), 770–780.
- 1058 Gavete, L., Gavete, M., & Benito, J. (2003). Improvements of generalized finite difference method and comparison with other meshless method. *Applied Mathematical Modelling*, 27(10), 831–847.
- 1059 Geiger, H. D., & Daley, P. F. (2003). Finite difference modelling of the full acoustic wave equation in matlab.
- 1060 Handoyo, H., Alcalde, J., DeFelipe, I., Palomeras, I., Martín-Banda, R., García-Mayordomo, J., Martí, D., Martínez-Díaz, J. J., Insua-Arévalo, J. M., Teixidó, T., et al. (2022). Geophysical imaging of the critical zone along the eastern betic shear zone (ebsz), se iberian peninsula. *Applied Sciences*, 12(7), 3398.
- 1061 Herrman, R. (2013). Computer programs in seismology: An evolving tool for instructijn and researcher.(2003) seism. *Res. Let.*, 84(6), 1081–1088.
- 1062 Holbrook, W. S., Marcon, V., Bacon, A. R., Brantley, S. L., Carr, B. J., Flinchum, B. A., Richter, D. D., & Riebe, C. S. (2019). Links between physical and chemical weathering inferred from a 65-m-deep borehole through earth's critical zone. *Scientific Reports*, 9(1), 4495.
- 1063 Holbrook, W. S., Riebe, C. S., Elwaseif, M., L. Hayes, J., Basler-Reeder, K., L. Harry, D., Malazian, A., Dosseto, A., C. Hartsough, P., & W. Hopmans, J. (2014). Geophysical constraints on deep weathering and water storage potential in the southern sierra critical zone observatory. *Earth Surface Processes and Landforms*, 39(3), 366–380.
- 1064 Huang, C., Shao, M., & Tan, W. (2011). Soil shrinkage and hydrostructural characteristics of three swelling soils in shaanxi, china. *Journal of Soils and Sediments*, 11, 474–481.
- 1065 Huiskamp, G. (1991). Difference formulas for the surface laplacian on a triangulated surface. *Journal of computational physics*, 95(2), 477–496.
- 1066 Ivanov, J., Tsolfias, G., Miller, R. D., Peterie, S., Morton, S., & Xia, J. (2016). Impact of density information on rayleigh surface wave inversion results. *Journal of Applied Geophysics*, 135, 43–54.
- 1067 James, S., Knox, H., Abbott, R., Panning, M., & Screamton, E. (2019). Insights into permafrost and seasonal active-layer dynamics from ambient seismic noise monitoring. *Journal of Geophysical Research: Earth Surface*, 124(7), 1798–1816.
- 1068 Jeong, W., Lee, H.-Y., & Min, D.-J. (2012). Full waveform inversion strategy for density in the frequency domain. *Geophysical Journal International*, 188(3), 1221–1242.
- 1069 Johnson, L. R. (1974). Green's function for lamb's problem. *Geophysical Journal International*, 37(1), 99–131.
- 1070 Karato, S.-i., & Karki, B. B. (2001). Origin of lateral variation of seismic wave velocities and density in the deep mantle. *Journal of Geophysical Research: Solid Earth*, 106(B10), 21771–21783.
- 1071 Kaufman, A. A., Levshin, A. L., & Larner, K. L. (2000). *Acoustic and elastic wave fields in geophysics* (Vol. 2). Gulf Professional Publishing.
- 1072 Köhn, D., De Nil, D., Kurzmann, A., Przebindowska, A., & Bohlen, T. (2012). On the influence of model parametrization in elastic full waveform tomography. *Geophysical Journal International*, 191(1), 325–345.
- 1073 Lamb, H. (1904). I. on the propagation of tremors over the surface of an elastic solid. *Philosophical Transactions of the Royal Society of London. Series A, Containing papers of a mathematical or physical character*, 203(359-371), 1–42.
- 1074 Langston, C. A. (2007a). Wave gradiometry in the time domain. *Bulletin of the Seismological Society of America*, 97(3), 926–933. <https://doi.org/10.1785/0120060152>
- 1075 Langston, C. A. (2007b). Spatial gradient analysis for linear seismic arrays. *Bulletin of the Seismological Society of America*, 97(1B), 265–280. <https://doi.org/10.1785/0120060100>
- 1076 Langston, C. A. (2007c). Wave gradiometry in two dimensions. *Bulletin of the Seismological Society of America*, 97(2), 401–416. <https://doi.org/10.1785/0120060138>

- 1175 Lax, P. D., & Wendroff, B. (1964). Difference schemes for hy-1243  
 1176 perabolic equations with high order of accuracy. *Communications on pure and applied mathematics*, 17(3), 381–1245  
 1177 398. 1246
- 1178 Liang, C., Cao, F., Liu, Z., & Chang, Y. (2023). A review of 1247  
 1180 the wave gradiometry method for seismic imaging. *Earthquake 1248  
 1181 Science*, 36(3), 254–281. 1249
- 1182 Liang, C., & Langston, C. A. (2009). Wave gradiometry for 1250  
 1183 usarray: Rayleigh waves. *Journal of Geophysical Research: 1251  
 1184 Solid Earth*, 114(B2). 1252
- 1185 Lin, F.-C., Tsai, V. C., & Ritzwoller, M. H. (2012). The local 1253  
 1186 amplification of surface waves: A new observable to con-1254  
 1187 strain elastic velocities, density, and anelastic attenuation. 1255  
 1188 *Journal of Geophysical Research: Solid Earth*, 117(B6). 1256
- 1189 Liszka, T., & Orkisz, J. (1980). The finite difference method 1257  
 1190 at arbitrary irregular grids and its application in applied 1258  
 1191 mechanics. *Computers & Structures*, 11(1-2), 83–95. 1259
- 1192 Liu, Y., & Holt, W. E. (2015). Wave gradiometry and its 1260  
 1193 link with helmholtz equation solutions applied to usarray 1261  
 1194 in the eastern us. *Journal of Geophysical Research: Solid 1262  
 1195 Earth*, 120(8), 5717–5746. 1263
- 1196 Luo, J., & Wu, R.-S. (2018). Velocity and density reconstruc-1264  
 1197 tion based on scattering angle separation. *Pure and Applied 1265  
 1198 Geophysics*, 175, 4371–4387. 1266
- 1199 Madariaga, R. (2007). Seismic source theory. *Earthquake 1267  
 1200 seismology*, 4, 59–82. 1268
- 1201 Maeda, T., Nishida, K., Takagi, R., & Obara, K. (2016). Re-1269  
 1202 construction of a 2d seismic wavefield by seismic gradiom-1270  
 1203 etry. *Progress in Earth and Planetary Science*, 3(1), 1–1271  
 1204 17. 1272
- 1205 Miller, S. L., & Stewart, R. R. (1991). The relationship be-1273  
 1206 tween elastic-wave velocities and density in sedimentary 1274  
 1207 rocks: A proposal. *Crewes Res. Rep.*, 260–273. 1275
- 1208 Mooney, H. M. (1974). Some numerical solutions for lamb's 1276  
 1209 problem. *Bulletin of the Seismological Society of America*, 64(2), 473–491. 1278
- 1211 Mosca, I., Cobden, L., Deuss, A., Ritsema, J., & Trampert, J. 1279  
 1212 (2012). Seismic and mineralogical structures of the lower 1280  
 1213 mantle from probabilistic tomography. *Journal of Geophysical 1281  
 1214 Research: Solid Earth*, 117(B6). 1282
- 1215 Mujs, R., Holliger, K., & Robertsson, J. O. (2002). Pertur-1283  
 1216 bation analysis of an explicit wavefield separation scheme 1284  
 1217 for p-and s-waves. *Geophysics*, 67(6), 1972–1982. 1285
- 1218 Muyzert, E., & Snieder, R. (2000). An alternative parameter-1286  
 1219 isation for surface waves in a transverse isotropic medium. 1287  
 1220 *Physics of the Earth and Planetary Interiors*, 118(1-2), 1288  
 1221 125–133. 1289
- 1222 Nabighian, M. N., Ander, M., Grauch, V., Hansen, R., LaFehr, T., Li, Y., Pearson, W., Peirce, J., Phillips, J., & Ruder, M. (2005). Historical development of the gravity method in explorationhistorical development of gravity method. *Geophysics*, 70(6), 63ND–89ND. 1294
- 1227 Nakata, N., Gualtieri, L., & Fichtner, A. (2019). *Seismic ambient noise*. Cambridge University Press. 1296
- 1229 Nanko, K., Ugawa, S., Hashimoto, S., Imaya, A., Kobayashi, M., Sakai, H., Ishizuka, S., Miura, S., Tanaka, N., Takanashi, M., et al. (2014). A pedotransfer function for estimating bulk density of forest soil in japan affected by volcanic ash. *Geoderma*, 213, 36–45. 1301
- 1234 Neitzel, E. B. (1958). Seismic reflection records obtained by dropping a weight. *Geophysics*, 23(1), 58–80. 1303
- 1236 Nielson, T., Bradford, J., Holbrook, W. S., & Seyfried, M. (2021). The effect of aspect and elevation on critical zone architecture in the reynolds creek critical zone observatory: A seismic refraction study. *Frontiers in Water*, 3, 670524. 1307
- 1240 Nolet, G., et al. (1977). The upper mantle under western eu-1308  
 1241 rope inferred from the dispersion of rayleigh modes. *Journal of Geophysics*, 43(1), 265–285. 1309
- 1242 Oakley, D. O., Forsythe, B., Gu, X., Nyblade, A. A., & Brantley, S. L. (2021). Seismic ambient noise analyses reveal changing temperature and water signals to 10s of meters depth in the critical zone. *Journal of Geophysical Research: Earth Surface*, 126(2), e2020JF005823. 1310
- Obermann, A., Kraft, T., Larose, E., & Wiemer, S. (2015). Potential of ambient seismic noise techniques to monitor the st. galen geothermal site (switzerland). *Journal of Geophysical Research: Solid Earth*, 120(6), 4301–4316.
- Operto, S., & Miniussi, A. (2018). On the role of density and attenuation in three-dimensional multiparameter viscoacoustic VTI frequency-domain FWI: an OBC case study from the North Sea. *Geophysical Journal International*, 213(3), 2037–2059. <https://doi.org/10.1093/gji/ggy103>
- Pan, L., Chen, X., Wang, J., Yang, Z., & Zhang, D. (2019). Sensitivity analysis of dispersion curves of rayleigh waves with fundamental and higher modes. *Geophysical Journal International*, 216(2), 1276–1303.
- Pan, W., Geng, Y., & Innanen, K. A. (2018). Interparameter trade-off quantification and reduction in isotropic-elastic full-waveform inversion: Synthetic experiments and hussar land data set application. *Geophysical Journal International*, 213(2), 1305–1333.
- Parsekian, A., Singha, K., Minsley, B. J., Holbrook, W. S., & Slater, L. (2015). Multiscale geophysical imaging of the critical zone. *Reviews of Geophysics*, 53(1), 1–26.
- Pekeris, C. (1955). The seismic surface pulse. *Proceedings of the national academy of sciences*, 41(7), 469–480.
- Piccolroaz, S., Majone, B., Palmieri, F., Cassiani, G., & Bellini, A. (2015). On the use of spatially distributed, time-lapse microgravity surveys to inform hydrological modeling. *Water Resources Research*, 51(9), 7270–7288.
- Plonka, A., Blom, N., & Fichtner, A. (2016). The imprint of crustal density heterogeneities on regional seismic wave propagation. *Solid Earth*, 7(6), 1591–1608.
- Prieux, V., Brossier, R., Operto, S., & Virieux, J. (2013). Multiparameter full waveform inversion of multicomponent ocean-bottom-cable data from the valhall field. part 1: Imaging compressional wave speed, density and attenuation. *Geophysical Journal International*, 194(3), 1640–1664.
- Qiao, J., Zhu, Y., Jia, X., Huang, L., & Shao, M. (2019). Development of pedotransfer functions for predicting the bulk density in the critical zone on the loess plateau, china. *Journal of soils and sediments*, 19, 366–372.
- Resovsky, J., & Trampert, J. (2003). Using probabilistic seismic tomography to test mantle velocity–density relationships. *Earth and Planetary Science Letters*, 215(1-2), 121–134.
- Riebe, C. S., Hahm, W. J., & Brantley, S. L. (2017). Controls on deep critical zone architecture: A historical review and four testable hypotheses. *Earth Surface Processes and Landforms*, 42(1), 128–156.
- Robertsson, J. O., & Curtis, A. (2002). Wavefield separation using densely deployed three-component single-sensor groups in land surface-seismic recordings. *Geophysics*, 67(5), 1624–1633.
- Robertsson, J. O., & Kragh, E. (2002). Rough-sea deghosting using a single streamer and a pressure gradient approximation. *Geophysics*, 67(6), 2005–2011.
- Robertsson, J. O., Levander, A., Symes, W. W., & Holliger, K. (1995). A comparative study of free-surface boundary conditions for finite-difference simulation of elastic/viscoelastic wave propagation. In *Seg technical program expanded abstracts 1995* (pp. 1277–1280). Society of Exploration Geophysicists.
- Robertsson, J. O., & Muyzert, E. (1999). Wavefield separation using a volume distribution of three component

- 1311 recordings. *Geophysical Research Letters*, 26(18), 2821–1352  
 1312 2824.
- 1313 Schmelzbach, C., Donner, S., Igel, H., Sollberger, D., 1354  
 1314 Taufiqurrahman, T., Bernauer, F., Häusler, M., Van 1355  
 1315 Renterghem, C., Wassermann, J., & Robertsson, J. (2018). 1356  
 1316 Advances in 6c seismology: Applications of combined 1357  
 1317 translational and rotational motion measurements in 1358  
 1318 global and exploration seismologyadvances in 6c seismol-1359  
 1319 ogy. *Geophysics*, 83(3), WC53–WC69. 1360
- 1320 Semblat, J., & Pecker, A. (2009). Waves and vibrations in 1361  
 1321 soils. *Earthquakes, traffic, shocks*, 13. 1362
- 1322 Shaiban, A., De Ridder, S., & Curtis, A. (2022). Wavefield 1363  
 1323 reconstruction and wave equation inversion for seismic 1364  
 1324 surface waves. *Geophysical Journal International*, 229(3), 1365  
 1325 1870–1880. 1366
- 1326 Shapiro, N., Campillo, M., Margerin, L., Singh, S., Kos-1367  
 1327 toglodov, V., & Pacheco, J. (2000). The energy partition-1368  
 1328 ing and the diffusive character of the seismic coda. *Bulletin1369*  
 1329 of the Seismological Society of America
- 1330 Shearer, P. M. (2019). *Introduction to seismology*. Cambridge1371  
 1331 university press. 1372
- 1332 Sollberger, D., Bradley, N., Edme, P., & Robertsson, J. O. 1373  
 1333 (2023). Efficient wave type fingerprinting and filtering by 1374  
 1334 six-component polarization analysis. *Geophysical Journal1375*  
 1335 International
- 1336 Sollberger, D., Igel, H., Schmelzbach, C., Edme, P., Van 1377  
 1337 Manen, D.-J., Bernauer, F., Yuan, S., Wassermann, J., 1378  
 1338 Schreiber, U., & Robertsson, J. O. (2020). Seismological1379  
 1339 processing of six degree-of-freedom ground-motion data. 1380  
 1340 *Sensors*, 20(23), 6904. 1381
- 1341 Sollberger, D., Schmelzbach, C., Robertsson, J. O., Green-1382  
 1342 halgh, S. A., Nakamura, Y., & Khan, A. (2016). The shal-1383  
 1343 low elastic structure of the lunar crust: New insights from 1384  
 1344 seismic wavefield gradient analysis. *Geophysical Research1385*  
 1345 *Letters*, 43(19), 10–078. 1386
- 1346 Suuster, E., Ritz, C., Roostalu, H., Reintam, E., Kõlli, R., & 1387  
 1347 Astover, A. (2011). Soil bulk density pedotransfer func-1388  
 1348 tions of the humus horizon in arable soils. *Geoderma*, 1389  
 1349 163(1-2), 74–82. 1390
- 1350 Takeuchi, H., & Saito, M. (1972). Seismic surface waves.  
*Methods in computational physics*, 11, 217–295.
- Tanimoto, T. (1991). Waveform inversion for three-dimensional density and s wave structure. *Journal of Geophysical Research: Solid Earth*, 96(B5), 8167–8189.
- Trampert, J., Deschamps, F., Resovsky, J., & Yuen, D. (2004). Probabilistic tomography maps chemical heterogeneities throughout the lower mantle. *Science*, 306(5697), 853–856.
- Trichandi, R., Bauer, K., Ryberg, T., Scherler, D., Bataille, K., & Krawczyk, C. M. (2022). Combined seismic and borehole investigation of the deep granite weathering structure—santa gracia reserve case in chile. *Earth Surface Processes and Landforms*, 47(14), 3302–3316.
- Tuckwell, G., Grossey, T., Owen, S., & Stearns, P. (2008). The use of microgravity to detect small distributed voids and low-density ground. *Quarterly Journal of Engineering Geology and Hydrogeology*, 41(3), 371–380.
- Vantassel, J. P., Kumar, K., & Cox, B. R. (2022). Using convolutional neural networks to develop starting models for near-surface 2-d full waveform inversion. *Geophysical Journal International*, 231(1), 72–90.
- Virieux, J., & Operto, S. (2009). An overview of full-waveform inversion in exploration geophysics. *Geophysics*, 74(6), WCC1–WCC26.
- Vossen, R. v., Trampert, J., & Curtis, A. (2004). Propagator and wave-equation inversion for near-receiver material properties. *Geophysical Journal International*, 157(2), 796–812.
- Wielandt, E. (1993). Propagation and Structural Interpretation of Non-Plane Waves. *Geophysical Journal International*, 113(1), 45–53. <https://doi.org/10.1111/j.1365-246X.1993.tb02527.x>
- Wu, G.-x., Pan, L., Wang, J.-n., & Chen, X. (2020). Shear velocity inversion using multimodal dispersion curves from ambient seismic noise data of usarray transportable array. *Journal of Geophysical Research: Solid Earth*, 125(1), e2019JB018213.
- Yuan, Y. O., Simons, F. J., & Bozdağ, E. (2015). Multiscale adjoint waveform tomography for surface and body waves. *Geophysics*, 80(5), R281–R302.

1391 **Appendix**

1392 **A Finite Difference Error**

1393 Throughout this analysis we use 2<sup>nd</sup> order accurate formulations of the finite difference approximation of  
 1394 the 2<sup>nd</sup> spatial derivative of the wavefield quantity  $\vartheta$ :

$$\frac{\partial^2 \vartheta}{\partial x^2} = \frac{\vartheta(x - \Delta x) - 2\vartheta(x) + \vartheta(x + \Delta x)}{\Delta x^2} - \frac{\Delta x^2}{24} \frac{\partial^4 \vartheta}{\partial x^4} \quad (\text{A1})$$

1395 Following (Langston, 2007b) we can calculate the error of this approximation due to the sampling for a  
 1396 sinusoidal wave by assuming a plane wave in the form

$$\vartheta(x, t) = e^{i\omega(t - \frac{x}{c})} \quad (\text{A2})$$

1397 We can then calculate the error  $\varepsilon$  based on the following formulation:

$$\varepsilon = \left| \frac{-\frac{\Delta x^2}{24} \frac{\partial^4 \vartheta}{\partial x^4}}{\frac{\partial^2 \vartheta}{\partial x^2}} \right| = \frac{\Delta x^2 (2\pi)^2}{24 \lambda^2} \quad (\text{A3})$$

1398 Setting an accuracy threshold  $\zeta$  for the second derivative, the condition

$$\varepsilon \leq \zeta \Leftrightarrow \Delta x \leq \sqrt{\frac{\zeta 24 \lambda^2}{(2\pi)^2}} \quad (\text{A4})$$

1399 implies the spacing  $\Delta x$  needs to be at most  $0.247 \lambda$  to ensure an error lower than  $\zeta = 0.1$ .

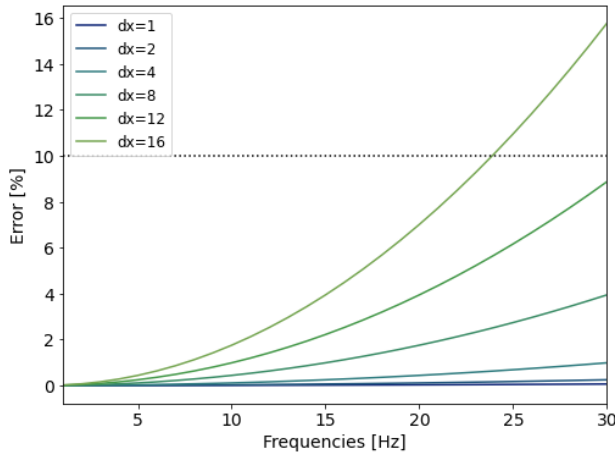


**Figure A1:** Error evolution of the used Finite Difference approximation with frequency for different receiver spacings given in m. Black dotted line shows threshold error of 10 %.

1400 **B Reference Density Model**

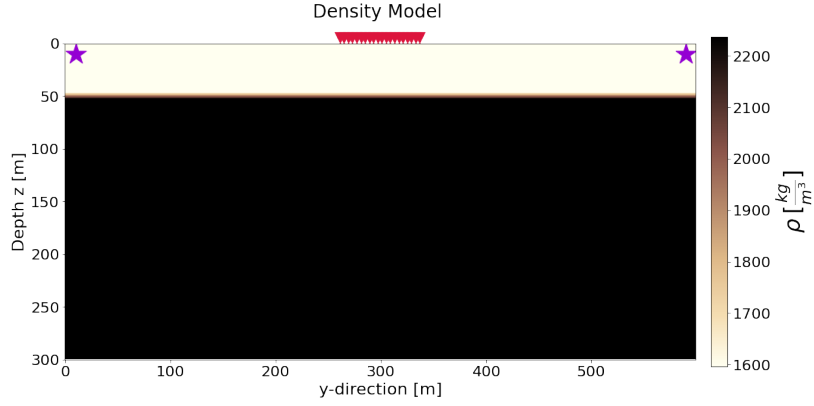


**Figure B1:** Reference density model depth cross-section in  $yz$ -plane. A constant density of  $1600 \text{ kg/m}^3$  is used for the top layer instead of the variable density structure imposed in Figure 3c and 3d.  $1600 \text{ kg/m}^3$  corresponds to the mean value of the top layer in the variable density model.

1401

1402 **C Frequency Dependence of Absolute Density Estimate**

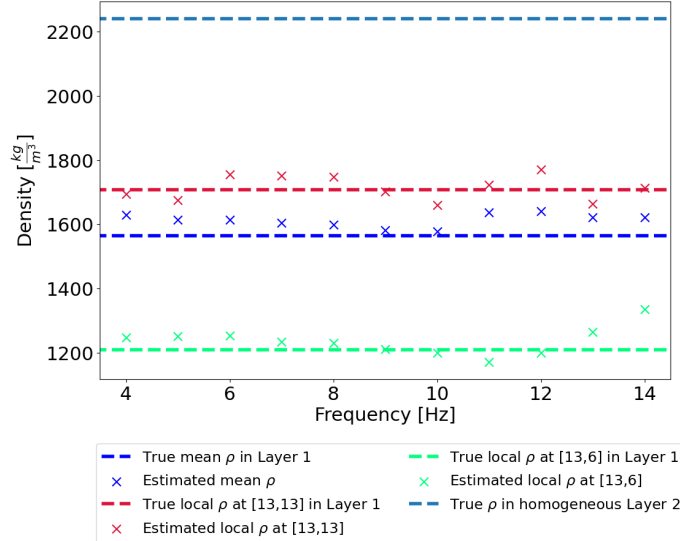


**Figure C1:** Frequency dependence of absolute density estimates obtained from full acoustic wave equation inversion. True model values shown at two local stations highlighted in Figure 9 e.g., [13,13] (green dotted line) and [13,6] (red dotted line) and as a mean over all stations (dark blue dotted line). Estimates are shown as crosses in the respective corresponding colours. The light blue dotted line shows the density value of layer 2.

1403 D Acoustic Parallel Velocity and Density Gradient Models

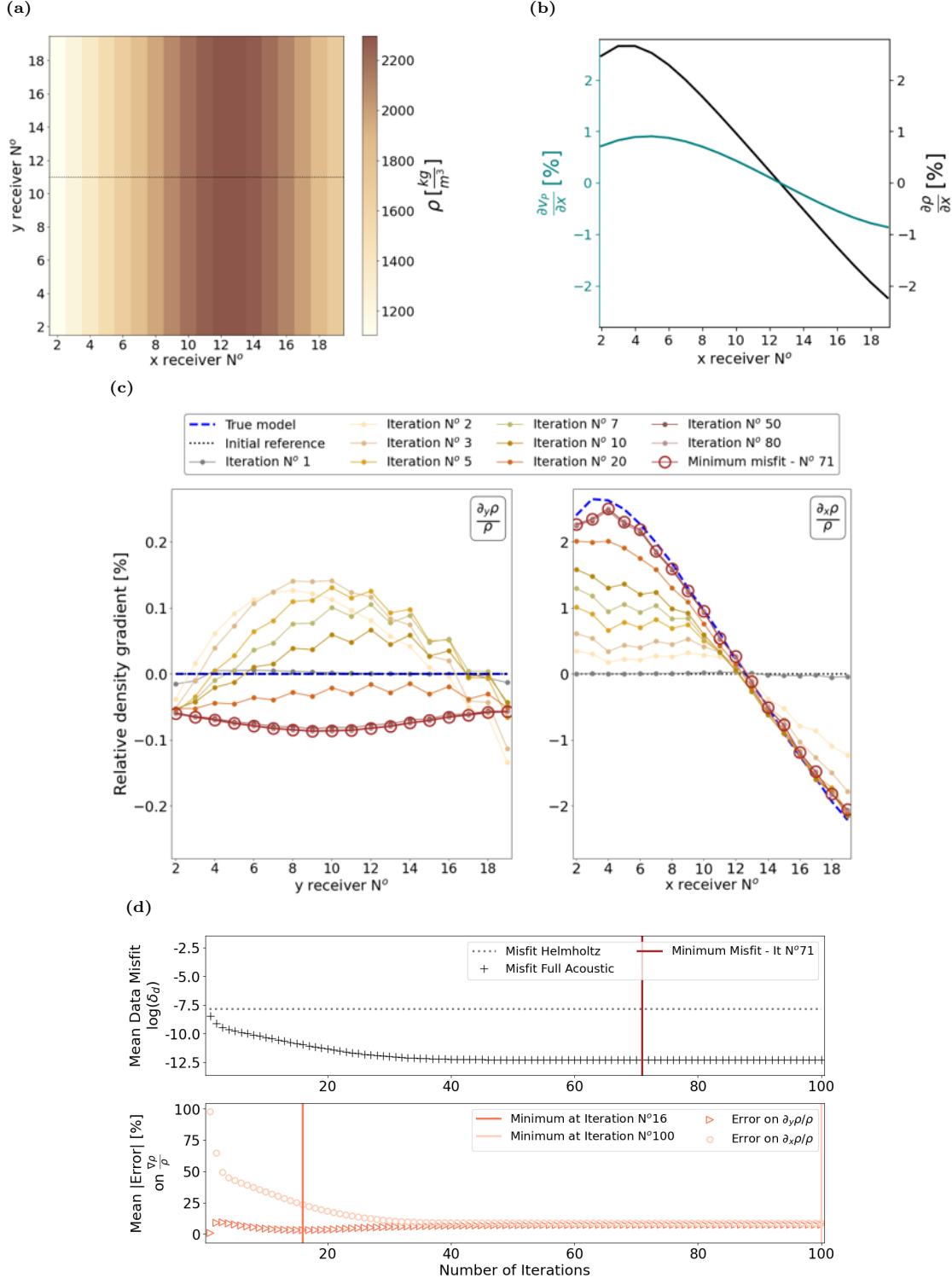


**Figure D1:** (a) True density model. Dotted black line shows direction of transect shown in panel (b). (b) True velocity and density structure highlighting the alignment of the gradients. Both velocity and density gradients follow the same sine curve but have different amplitudes. (c) Idem Fig. 6(b) (d) Idem Fig. 6(c) with minimum misfit at iteration 100, and minimum parameter error on relative density y- and x-gradients at iteration 16 and 100, respectively.

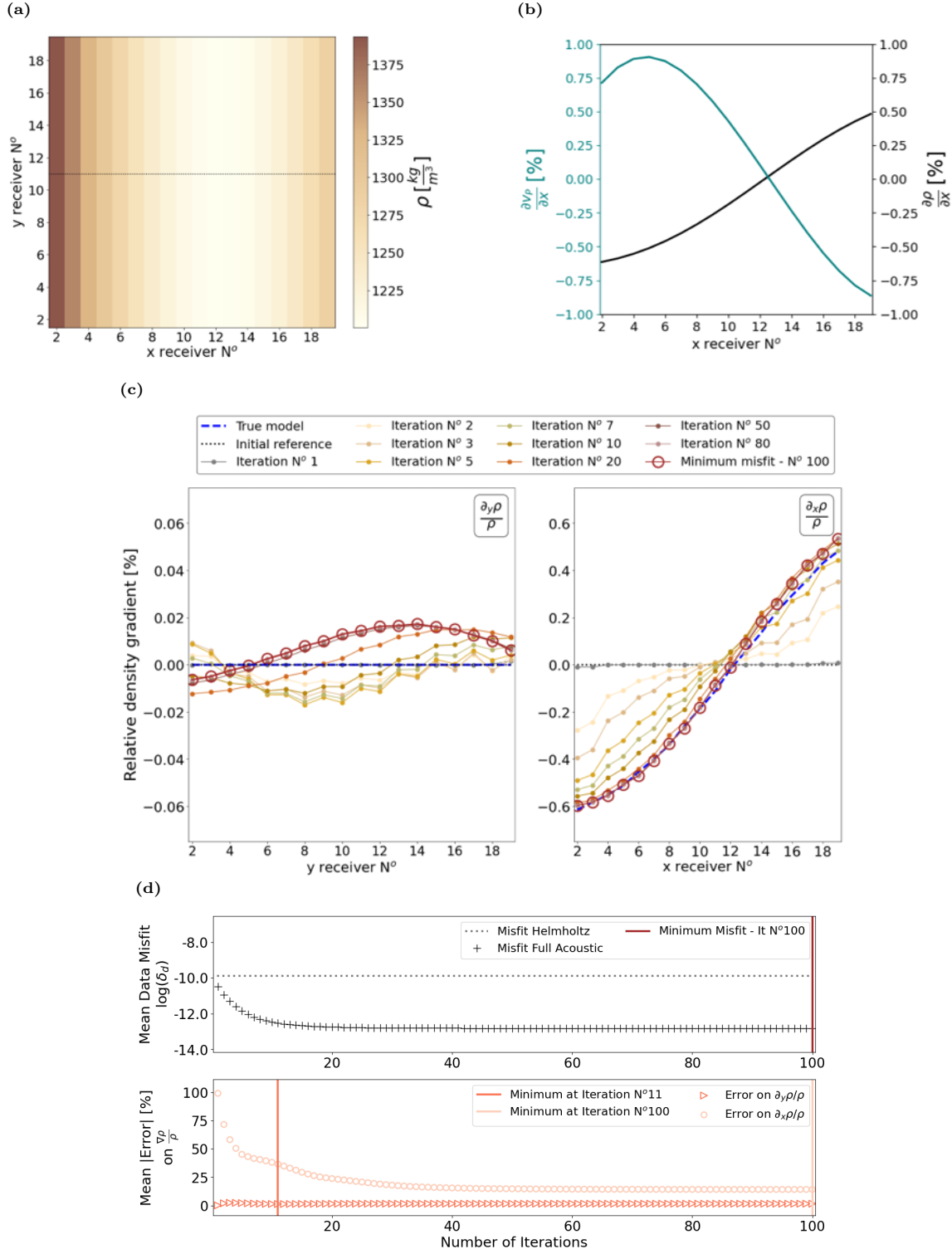


**Figure D2:** (a) True density model. Dotted black line shows direction of transect shown in panel (b). (b) True velocity and density structure highlighting the alignment of the gradients. Both velocity and density gradients are shifted in respect to each other but have similar amplitudes. (c) and Idem Fig. 6(b). (d) Idem Fig. 6(c) with minimum misfit at iteration 100, and minimum parameter error on relative density y- and x-gradients at iteration 11 and 100, respectively.

1404 **E Notes on the free surface methodology in inhomogeneous elastic media**

1405 In the body of this manuscript, all derivations from Newton's second law in equation (1) are based on the  
 1406 assumption that Lamé parameters are constant over space (eq. 2a in elastic media and eq. 2b in acoustic  
 1407 media). For laterally varying Lamé parameters, these equations become:

$$\underbrace{\frac{(\lambda + 2\mu)}{\rho} [\nabla(\nabla \cdot \mathbf{u})] - \frac{\mu}{\rho} [\nabla \times (\nabla \times \mathbf{u})]}_{\text{homogeneous terms}} + \underbrace{\frac{\nabla \lambda}{\rho} (\nabla \cdot \mathbf{u}) + \frac{\nabla \mu}{\rho} \cdot [\nabla \mathbf{u} + (\nabla \mathbf{u})^T]}_{\text{inhomogeneous terms}} + \frac{\mathbf{f}}{\rho} = \partial_t^2 \mathbf{u} \quad (\text{E1a})$$

$$\underbrace{\frac{\lambda}{\rho} [\nabla(\nabla \cdot \mathbf{u})]}_{\text{homogeneous terms}} + \underbrace{\frac{\nabla \lambda}{\rho} (\nabla \cdot \mathbf{u})}_{\text{inhomogeneous terms}} + \frac{\mathbf{f}}{\rho} = \partial_t^2 \mathbf{u} \quad (\text{E1b})$$

1408 Here we investigate the effect that inhomogeneity has on the derivation of the equations in the free surface  
 1409 methodology used to estimate density and body wave velocities at the free surface presented in Section (2).  
 1410 Writing (E1a) with all terms:

$$\begin{aligned} & \underbrace{\frac{(\lambda + 2\mu)}{\rho} \left( \begin{array}{c} \frac{\partial^2 u_x}{\partial x^2} + \frac{\partial^2 u_y}{\partial x \partial y} + \frac{\partial^2 u_z}{\partial x \partial z} \\ \frac{\partial^2 u_x}{\partial y \partial x} + \frac{\partial^2 u_y}{\partial^2 y} + \frac{\partial^2 u_z}{\partial y \partial z} \\ \frac{\partial^2 u_x}{\partial z \partial x} + \frac{\partial^2 u_y}{\partial z \partial y} + \frac{\partial^2 u_z}{\partial^2 z} \end{array} \right)}_{\text{homogeneous terms}} - \frac{\mu}{\rho} \left( \begin{array}{c} \frac{\partial^2 u_y}{\partial y \partial x} - \frac{\partial^2 u_x}{\partial^2 y} - \frac{\partial^2 u_x}{\partial^2 z} + \frac{\partial^2 u_z}{\partial x \partial z} \\ \frac{\partial^2 u_z}{\partial z \partial y} - \frac{\partial^2 u_y}{\partial^2 z} - \frac{\partial^2 u_y}{\partial^2 x} + \frac{\partial^2 u_x}{\partial x \partial y} \\ \frac{\partial^2 u_x}{\partial x \partial z} - \frac{\partial^2 u_z}{\partial^2 x} - \frac{\partial^2 u_z}{\partial^2 y} + \frac{\partial^2 u_y}{\partial y \partial z} \end{array} \right) \\ & + \underbrace{\frac{1}{\rho} \left( \begin{array}{c} \frac{\partial \lambda}{\partial x} \\ \frac{\partial \lambda}{\partial y} \\ \frac{\partial \lambda}{\partial z} \end{array} \right) \left( \frac{\partial u_x}{\partial x} + \frac{\partial u_y}{\partial y} + \frac{\partial u_z}{\partial z} \right) + \frac{1}{\rho} \left( \begin{array}{c} \frac{\partial \mu}{\partial x} \\ \frac{\partial \mu}{\partial y} \\ \frac{\partial \mu}{\partial z} \end{array} \right) \cdot \left[ \begin{array}{ccc} \frac{\partial u_x}{\partial x} & \frac{\partial u_x}{\partial y} & \frac{\partial u_x}{\partial z} \\ \frac{\partial u_y}{\partial x} & \frac{\partial u_y}{\partial y} & \frac{\partial u_y}{\partial z} \\ \frac{\partial u_z}{\partial x} & \frac{\partial u_z}{\partial y} & \frac{\partial u_z}{\partial z} \end{array} \right]}_{\text{inhomogeneous terms}} + \left[ \begin{array}{ccc} \frac{\partial u_x}{\partial x} & \frac{\partial u_y}{\partial x} & \frac{\partial u_z}{\partial x} \\ \frac{\partial u_x}{\partial y} & \frac{\partial u_y}{\partial y} & \frac{\partial u_z}{\partial y} \\ \frac{\partial u_x}{\partial z} & \frac{\partial u_y}{\partial z} & \frac{\partial u_z}{\partial z} \end{array} \right] \\ & = \left( \begin{array}{c} \frac{\partial^2 u_x}{\partial t^2} \\ \frac{\partial^2 u_y}{\partial t^2} \\ \frac{\partial^2 u_z}{\partial t^2} \end{array} \right) - \frac{1}{\rho} \left( \begin{array}{c} f_x \\ f_y \\ f_z \end{array} \right) \end{aligned} \quad (\text{E2})$$

<sup>1411</sup> we can use the free surface conditions

$$\frac{\partial u_z}{\partial z} = -\frac{v_p^2 - 2v_s^2}{v_p^2} \left( \frac{\partial u_x}{\partial x} + \frac{\partial u_y}{\partial y} \right) \quad (\text{E3})$$

$$\frac{\partial u_y}{\partial z} = -\frac{\partial u_z}{\partial y} \quad (\text{E4})$$

$$\frac{\partial u_x}{\partial z} = -\frac{\partial u_z}{\partial x} \quad (\text{E5})$$

<sup>1412</sup> to derive the corresponding expression at the free surface. The expression of the homogeneous terms are  
<sup>1413</sup> described in (Curtis and Robertsson, 2002) and the inhomogeneous terms become:

- <sup>1414</sup> • Term 3 of eq.(E3)

$$\frac{1}{\rho} \begin{pmatrix} \frac{\partial \lambda}{\partial x} \\ \frac{\partial \lambda}{\partial y} \\ \frac{\partial \lambda}{\partial z} \end{pmatrix} \left( \frac{\partial u_x}{\partial x} + \frac{\partial u_y}{\partial y} - \frac{v_p^2 - 2v_s^2}{v_p^2} (\nabla_H \cdot \mathbf{u}_H) \right) \quad (\text{E6})$$

- <sup>1415</sup> • Term 4 of eq.(E3)

$$\frac{1}{\rho} \begin{pmatrix} \frac{\partial \mu}{\partial x} \\ \frac{\partial \mu}{\partial y} \\ \frac{\partial \mu}{\partial z} \end{pmatrix} \cdot \begin{pmatrix} \frac{2\partial u_x}{\partial x} & \frac{\partial u_x}{\partial y} + \frac{\partial u_y}{\partial x} & \frac{\partial u_x}{\partial z} + \frac{\partial u_z}{\partial x} \\ \frac{\partial u_y}{\partial x} + \frac{\partial u_x}{\partial y} & 2\frac{\partial u_y}{\partial y} & \frac{\partial u_y}{\partial z} + \frac{\partial u_z}{\partial y} \\ \frac{\partial u_z}{\partial x} + \frac{\partial u_x}{\partial z} & \frac{\partial u_z}{\partial y} + \frac{\partial u_y}{\partial z} & 2\frac{\partial u_z}{\partial z} \end{pmatrix} \quad (\text{E7})$$

$$= \frac{1}{\rho} \begin{pmatrix} \frac{\partial \mu}{\partial x} \\ \frac{\partial \mu}{\partial y} \\ \frac{\partial \mu}{\partial z} \end{pmatrix} \cdot \begin{pmatrix} \frac{2\partial u_x}{\partial x} & \frac{\partial u_x}{\partial y} + \frac{\partial u_y}{\partial x} & -\frac{\partial u_z}{\partial x} + \frac{\partial u_z}{\partial x} \\ \frac{\partial u_y}{\partial x} + \frac{\partial u_x}{\partial y} & 2\frac{\partial u_y}{\partial y} & -\frac{\partial u_z}{\partial y} + \frac{\partial u_z}{\partial y} \\ \frac{\partial u_z}{\partial x} - \frac{\partial u_x}{\partial x} & \frac{\partial u_z}{\partial y} - \frac{\partial u_y}{\partial z} & -2\frac{v_p^2 - 2v_s^2}{v_p^2} \nabla_H \cdot \mathbf{u}_H \end{pmatrix} \quad (\text{E8})$$

$$= \frac{1}{\rho} \begin{pmatrix} \left[ \frac{\partial \mu}{\partial x} \left( \frac{2\partial u_x}{\partial x} \right) \right] + \left[ \frac{\partial \mu}{\partial y} \left( \frac{\partial u_x}{\partial y} + \frac{\partial u_y}{\partial x} \right) \right] + 0 \\ \left[ \frac{\partial \mu}{\partial x} \left( \frac{\partial u_y}{\partial x} + \frac{\partial u_x}{\partial y} \right) \right] + \left[ \frac{\partial \mu}{\partial y} \left( 2\frac{\partial u_y}{\partial y} \right) \right] + 0 \\ 0 + 0 + \left[ \frac{\partial \mu}{\partial z} \left( -2\frac{v_p^2 - 2v_s^2}{v_p^2} \nabla_H \cdot \mathbf{u}_H \right) \right] \end{pmatrix} \quad (\text{E9})$$

<sup>1416</sup> In our model, the receiver is buried at 1 m and the Lamé parameters do not change over the depth interval  
<sup>1417</sup> used for the calculation of the finite difference approximation of the first order depth derivative. We can  
<sup>1418</sup> thus consider the depth derivatives of Lamé parameters  $\partial \mu / \partial z$  and  $\partial \lambda / \partial z$  to be zero, and the inhomogeneous

<sup>1419</sup> terms disappear in the vertical component of the full elastic wave equation at the free surface.